TITLE

Systematic genetic characterization of the human PKR kinase domain highlights its functional malleability to escape a poxvirus substrate mimic

AUTHORS

Michael J. Chambers (1,2), Sophia B. Scobell (1), Meru J. Sadhu (1)

AFFILIATIONS

1. Center for Genomics and Data Science Research, National Human Genome Research Institute, National Institutes of Health, Bethesda, Maryland, USA
2. Department of Microbiology & Immunology, Georgetown University, Washington DC, USA

ABSTRACT

Evolutionary arms races can arise at the contact surfaces between host and viral proteins, producing dynamic spaces in which genetic variants are continually pursued. However, the sampling of genetic variation must be balanced with the need to maintain protein function. A striking case is given by protein kinase R (PKR), a member of the mammalian innate immune system. PKR detects viral replication within the host cell and halts protein synthesis to prevent viral replication by phosphorylating eIF2α, a component of the translation initiation machinery. PKR is targeted by many viral antagonists, including poxvirus pseudosubstrate antagonists that mimic the natural substrate, eIF2α, and inhibit PKR activity. Remarkably, PKR has several rapidly evolving residues at this interface, suggesting it is engaging in an evolutionary arms race, despite the surface's critical role in phosphorylating eIF2α. To systematically explore the evolutionary opportunities available at this dynamic interface, we generated and characterized a library of 426 SNP-accessible nonsynonymous variants of human PKR for their ability to escape inhibition by the model pseudosubstrate inhibitor K3, encoded by the vaccinia virus gene *K3L*. We identified key sites in the PKR kinase domain that harbor K3-resistant variants, as well as critical sites where variation leads to loss of function. We find K3-resistant variants are readily available throughout the interface and are enriched at sites under positive selection. Moreover, variants beneficial against K3 were also beneficial against an enhanced variant of K3, indicating resilience to viral adaptation. Overall, we find that the eIF2α-binding surface of PKR is highly malleable, potentiating its evolutionary ability to combat viral inhibition.

33 **INTRODUCTION**

34 Molecular interfaces between interacting host and pathogen proteins are atomic
35 battlegrounds that give rise to evolutionary arms races (1). Successful infection typically
36 involves critical interactions between host and pathogen proteins, such as binding to cell-
37 surface receptors or inhibition of cellular defense mechanisms. In such scenarios, the host
38 benefits from genetic mutations that disrupt the interaction while the pathogen benefits from
39 mutations that maintain the interaction. The pursuit of genetic mutations by the host and
40 pathogen can develop into an evolutionary arms race where the accumulation of mutations
41 leads to abnormally high sequence diversity, which is used to identify sites experiencing positive
42 selection.

43 A key member of the antiviral innate immune repertoire in vertebrates is protein kinase R
44 (PKR) (2–4). PKR contains two N-terminal double-stranded RNA (dsRNA) binding domains and
45 a C-terminal kinase domain, separated by a long linker (5). The presence of dsRNA in the
46 cytoplasm is a hallmark of viral infection (6). PKR binds dsRNA, initiating PKR
47 homodimerization and autophosphorylation, which activates the kinase (7–10). Active PKR
48 binds and phosphorylates eIF2α on Ser51 (Figure 1A), a member of the translation initiation
49 machinery. Phosphorylation of eIF2α leads to a halt in protein synthesis, thereby preventing
50 viral replication (8,11,12).

51 Vertebrate PKR homologs have many sites under positive selection (13), including
52 residues at its binding surface with eIF2α (Figure 1B). This is remarkable given the critical
53 nature of this interface and that eIF2α is an unvarying protein under purifying selection (14).
54 Many viruses encode PKR inhibitors to evade its antiviral activity, some of which are known to
55 interact with PKR at its eIF2α-binding interface (15–17). One example is vaccinia virus, whose
56 well-characterized pseudosubstrate inhibitor protein K3 is encoded by the *K3L* gene (Figure 1C)
57 (18–20). Vaccinia K3 mimics the structure and sequence of eIF2α to inhibit PKR and prevent
58 the halt of protein synthesis (19,21–23). Thus, despite evolutionary pressure on PKR to

59 recognize the conserved eIF2α substrate, variation at the same interface would be evolutionarily
60 beneficial if it allowed evasion of viral pseudosubstrate antagonists. Indeed, previous studies
61 have identified some single-residue variants at sites under positive selection in the PKR kinase
62 domain that maintain recognition of eIF2α yet resist vaccinia K3 (13,14,24). However, without
63 comprehensively exploring the genetic landscape at this interface, it is unclear how readily PKR
64 can mutate to evade viral antagonists while preserving its kinase function.

65 Here we use a prospective, systematic, and unbiased approach to map SNP-accessible
66 PKR variants in the kinase domain that are resistant or susceptible to the vaccinia wild-type K3,
67 nonfunctional K3, and the enhanced mutant allele K3-H47R. We found many novel K3-resistant
68 variants, especially at sites under positive selection, and note a strong correlation between
69 variants that resist wild-type K3 and the enhanced allele. We also identified sites in the PKR
70 kinase domain where variants increased susceptibility to vaccinia K3. Essential PKR residues
71 that did not tolerate variation were infrequent despite the critical nature of this interface; they
72 were primarily found surrounding the ATP-binding site. These results paint a portrait of PKR
73 balancing the tension between conserved function and evasion of viral inhibitors through
74 mutational resilience in its substrate interface.

75

76 **RESULTS**

77 **Generation of nonsynonymous PKR variant library**

78 We systematically made genetic variants in four windows of interest in the kinase
79 domain of PKR (Figure 1D). The four windows were selected based on having sites within five
80 angstroms of eIF2α or K3 and sites under positive selection across vertebrate PKR homologs
81 as identified by Rothenburg et al. (13). Our windows of interest include helix αD and αG, as well
82 as the glycine-rich loop and activation loop surrounding the ATP-binding site. In these windows,
83 we focused on testing 426 variants that could be acquired with a single nucleotide change from

84 the predominant human PKR allele (Genbank M85294.1) (Supplemental Figure 1A), as those
85 are the most likely to be evolutionarily sampled.
86 Overexpression of PKR in the budding yeast *Saccharomyces cerevisiae* is toxic, as PKR
87 auto-activates and shuts down protein synthesis by phosphorylating yeast eIF2α, which is highly
88 conserved between yeast and humans (25,26). This toxicity can be partially counteracted by co-
89 expression of vaccinia K3 (23). Thus, yeast provides a useful experimental system to test the
90 functionality of PKR variants: variants that maintain the ability to phosphorylate eIF2α while
91 escaping K3 inhibition will further arrest growth, while variants that lose eIF2α kinase activity or
92 become more susceptible to K3 will improve growth.
93 We sought to leverage this assay in a high-throughput manner to determine the
94 functionality of PKR variants by tracking their abundances in a pool over time. We generated the
95 426 single-residue variants of PKR on a single-copy plasmid with a galactose-inducible
96 promoter in a plasmid pool (Figure 1E). Each unique plasmid in the pool carried a DNA barcode
97 randomly generated during cloning. We used long-read circular consensus sequencing to pair
98 DNA barcodes with PKR variants, identifying an average of 43 barcodes per variant
99 (Supplemental Figure 1B). We then created three libraries by combining the PKR variant library
100 with wild-type K3, nonfunctional K3, or the enhanced mutant allele K3-H47R (23,27). The K3
101 alleles were expressed from a constitutive *TDH3* promoter. We transformed the three PKR-K3
102 paired libraries in duplicate into yeast grown in glucose media, such that PKR expression was
103 repressed. We then inoculated the libraries in liquid galactose media to induce PKR expression,
104 and sampled cells at 0, 12, 16, and 20 hours post-inoculation. We quantified the abundance of
105 the PKR variants at each timepoint using high-throughput short-read sequencing of the DNA
106 barcodes. For each PKR variant we calculated a functional score against each K3: PKR variants
107 that evade K3 inhibition and reduce yeast growth have high functional scores, while PKR
108 variants that are non-functional or are inhibited by vaccinia K3, and thus are associated with
109 good yeast growth, have low functional scores (Supplemental Figure 2). The correlation of

110 functional scores between replicates 1 and 2 was very strong (Pearson correlation coefficient >
111 0.98 for each K3 allele, Supplemental Figure 3), so we combined the reads from replicates 1
112 and 2 to generate PKR functional scores for subsequent analyses.
113
114 **Many PKR variants evade K3 while maintaining kinase function**
115 We first examined how each PKR variant performed against wild-type K3. We were
116 encouraged to find that variants previously characterized as resistant to K3-H47R (24) were
117 resistant to wild-type K3 in our screen (Figure 2A). We found many additional K3-resistant
118 variants across all four tested windows and validated select PKR variants using serial dilution to
119 measure yeast growth (Supplemental Figure 4). Notably, every variant made at Glu375
120 increased evasion of K3, with the exception of Glu375Asp. In the AlphaFold2-predicted
121 complex, Glu375 forms an attractive electrostatic interaction with Lys45 of K3 (Figure 2B).
122 Consistent with our findings, this predicted interaction would be disrupted by all tested variants
123 at site 375 aside from the negatively charged aspartic acid. Interestingly, Glu375 is the only site
124 under positive selection in vertebrates that was proximal to K3 but not eIF2α in the AlphaFold2
125 models, making it a prime candidate for disrupting K3 inhibition without affecting eIF2α
126 phosphorylation.
127 We found a large number of K3-resistant variants in the vicinity of PKR's helix αG
128 (Figure 2C,D). Compared to other protein kinase structures, eIF2α kinases have a noncanonical
129 helix αG that is extended by one full turn and rotated 40° counterclockwise with a 5 angstrom
130 translation relative to its C-terminus, owing to a reduced αF-αG linker (5). The noncanonical
131 orientation of helix αG contributes to both eIF2α binding specificity and Ser51 presentation to
132 PKR (5). It has been proposed that mutations causing movement in helix αG might be especially
133 capable of disrupting K3 binding due to the rigid structure of K3 between its contact points on
134 helix αG and the PKR active site. In contrast, PKR mutations that move helix αG could be
135 tolerated in the context of eIF2α binding because eIF2α contacts PKR's active site using a

136 flexible loop (5). We observe a gradient of PKR functional scores along the helix αG region,
137 starting with highly resistant or susceptible variants (positions 480-492) and shifting to neutral
138 wild-type-like scores (493-500) (Figure 2A). We identified four sites within or near the N-
139 terminus of helix αG for which many variants evade K3: Glu480, Val484, Glu490, and Thr491
140 (Figure 2C).

141 We looked at what features of PKR were associated with sites of K3-resistant variants
142 and were excited to find that sites under positive selection in vertebrates were strongly enriched
143 for K3-resistant variants relative to sites conserved across vertebrate PKRs (Figure 2E).
144 Comparing K3 contact and non-contact sites, we find significantly lower functional scores at K3
145 contact sites (Figure 2F). However, functional scores at K3 contact sites form a bimodal
146 distribution (Hartigan's dip test statistic = 0.105, $p < 0.0001$). Considering only functional
147 variants (PKR functional score > -2) we find that variants at K3 contact sites have significantly
148 higher functional scores than those at non-contact sites (Supplemental Figure 5). Thus, variants
149 at K3 contact sites tend towards large effects either improving or diminishing PKR function
150 versus K3.

151

152 **Sampled sites in the PKR kinase domain are largely resilient to genetic variation**

153 To understand the constraint placed on the PKR kinase domain, we examined variants
154 that failed to maintain PKR function. We screened our PKR variant library against a
155 nonfunctional K3 (hereafter referred to as K3Δ58) in which the first 173 bases were deleted,
156 removing the first 58 residues, including the initial methionine. When paired with K3Δ58, most
157 PKR variants were comparable to wild-type PKR (Figure 3A), suggesting the tested regions
158 were not highly functionally constrained for kinase activity despite their proximity to eIF2α during
159 its phosphorylation. The few highly constrained sites include Gly276 and Gly277, which
160 compose the glycine-rich loop above the ATP-binding site; Gly450 and Thr451 in the activation
161 loop; and Thr487 in helix αG, which stabilizes helix αG (5) and induces the conformational

162 change in eIF2α required for its phosphorylation (Figure 3B) (28). We also found proline variants
163 to generally disrupt PKR function (Figure 3C). We found nonfunctional variants of varying
164 degrees in all four windows of interest, but with very few in helix αD and the C-terminus of helix
165 αG (Figure 3C), consistent with these regions having pliable secondary structures in which
166 variants can evade K3 while not disrupting eIF2α recognition.

167 More PKR variants had low functional scores in the presence of functional K3 (Figure
168 2A) than in its absence (Figure 3C). We plotted the functional scores against each other (Figure
169 4A), and found that variants with low PKR functional scores versus K3 separated into two
170 classes: some switched to high functional scores in the absence of K3, indicating they caused
171 enhanced susceptibility to K3 but otherwise retained PKR function, while others had low
172 functional scores in both conditions, indicating they had diminished eIF2α kinase activity
173 irrespective of K3 antagonism. We quantified this effect by calculating residuals from the line
174 connecting PKR nonsense variants to PKR-WT, which highlights variants whose functional
175 scores diverged between the K3 conditions. We find that the activation loop and the start of
176 helix αG, which were less tolerant of mutation when paired with wild-type K3 (Figure 2D),
177 contain a mix of variants that lose function outright or that increase susceptibility to K3 (Figures
178 3B-C, 4B-C). Variants at five sites were especially susceptible to K3 inhibition: Phe278, Thr373,
179 Arg453, Phe489, and Ser492 (Figure 4B). None appear under positive selection across
180 vertebrates, and Phe278 is conserved across vertebrate PKR homologs. Interestingly, Phe278
181 is predicted to form a pi interaction with His47 of K3, which aligns to Arg52 of eIF2α
182 (Supplemental Figure 6) (23). Mutation of K3-H47 to arginine, matching eIF2α, is known to
183 improve K3's antagonism of PKR (23,27), suggesting PKR can discriminate against K3 based
184 on its difference from eIF2α at this position. This is consistent with our observation of the
185 importance of Phe278 specifically in the presence of K3.

186

187 **K3-resistant variants were largely resistant to enhanced K3-H47R**

188 We also characterized PKR variants in the presence of an enhanced mutant allele of K3,
189 K3-H47R (Figure 5). This mutant allele was first identified in a genetic screen of K3 mutants as
190 an enhanced antagonist of PKR (23) and independently identified in a directed evolution screen
191 (27). We sought to understand the resilience of improved PKR variants to alternative K3 alleles
192 by examining the concordance between beneficial PKR variants against wild-type K3 and K3-
193 H47R. We found strong correlation between PKR functional scores versus K3 and K3-H47R
194 (Spearman correlation = 0.832, Figure 5A). Indeed, many of the K3-resistant variants are also
195 resistant to K3-H47R (Figure 5B-D), suggesting resilience of PKR to allelic variation in K3. A
196 general change is the struggle for PKR to overcome the enhanced inhibition of K3-H47R,
197 compressing the functional score range between wild-type-like and nonfunctional scores. This
198 nonlinear relationship between the functional scores in the two K3 conditions (Supplemental
199 Figure 7) led to some differences in the patterns of resistance to the two K3 alleles. For
200 instance, positively selected PKR sites did not have significantly higher PKR functional scores
201 versus K3-H47R than conserved sites (Figure 5E), a sharp contrast to the PKR functional
202 scores versus wild-type K3 (Figure 2E). This result appears to be caused by the many wild-type-
203 like scores at positively selected sites now being similar to the many nonsense-like scores at
204 conserved sites. We also noted that variants at sites proximal to K3 had slightly higher
205 functional scores than those at non-contact sites (Figure 5F), the opposite of what we observed
206 against wild-type K3 (Figure 2F). This could result from wild-type-like PKR variants being
207 enriched at non-contact sites. Overall, the strong correlation of functional scores versus K3 and
208 K3-H47R suggests K3-resistant variants would often be resilient against alternate K3 alleles.
209 Previous work identified twelve PKR variants with enhanced resistance to K3-H47R (24),
210 nine of which were included in our experiment (Supplemental Figure 8). We examined the other
211 nonsynonymous variants introduced at these sites and found that most sites contained
212 additional novel resistant variants, indicating the previously uncovered individual mutants reflect
213 sites of general opportunity for pseudosubstrate evasion.

214

215 **DISCUSSION**

216 Here we characterize the local evolutionary space available to the human innate
217 immunity protein PKR to maintain functionality while evading the well-studied vaccinia virus
218 antagonist, K3. One strategy viruses leverage against PKR is pseudosubstrate inhibition, in
219 which proteins like K3 bind PKR by structurally mimicking its natural substrate eIF2α, inhibiting
220 PKR kinase activity. Interestingly, this binding interface contains many residues under positive
221 selection. However, positively selected genetic variants across the binding interface would need
222 to maintain binding with PKR's natural substrate while evading viral pseudosubstrate
223 antagonists. In this study, we quantified the abundance of such "tightrope-walking" genetic
224 variants relative to the abundance of functionally deleterious variants, which highlighted
225 particular sites of opportunity and constraint within the kinase domain.

226 We identified many sites containing variants that evade vaccinia K3 without losing eIF2α
227 targeting. Resistant variants clustered around helices αD and αG, secondary structures with
228 sites under positive selection and where resistant variants have been previously characterized
229 (13,24). Overall, we found few genetic variants that impair the kinase function of PKR (Figure 3),
230 underscoring the genetic resilience of PKR, with functionally constrained sites mostly localized
231 to the vicinity of the ATP-binding site. Finally, we found a strong correlation between PKR
232 variants that are resistant against both K3 and the enhanced antagonist K3-H47R, suggesting
233 the K3-resistant variants are resilient to K3 allelic variation.

234 We identified sites across the PKR kinase domain that were K3-resistant, K3-
235 susceptible, or essential to eIF2α phosphorylation (Figure 6A). Sites enriched with genetic
236 variants that improve evasion of K3 were classified as K3-resistant sites, such as Glu375 and
237 Glu480. We find clusters of these sites located across helices αD and αG, at the binding surface
238 of K3 and eIF2α. Positive selection sites are enriched for K3-resistant variants. There were sites
239 under positive selection where we did not observe much K3 resistance, such as sites 269-272,

240 which may suggest this region is antagonized by a completely different viral antagonist. Still, we
241 found these sites to be generally able to adopt variants that maintain PKR function (Figure 3),
242 making them prime “tightrope-walking” sites for thwarting any alternate viral inhibitors that
243 interact at those sites. We also identified some K3-resistant sites that are not under positive
244 selection, such as Glu480, which is in fact conserved across vertebrate PKR homologs and the
245 four human eIF2α kinases (9,13). Perhaps it has an important role in a function not tested in our
246 assay, such as avoiding off-target phosphorylation of other human proteins.

247 Our analysis does not account for variation in PKR expression that may result from the
248 introduced variation. Previous work demonstrated that K3-resistant PKR variants were not
249 enhanced due to increased expression (13). We note that we did not observe much variation in
250 PKR functional scores in the absence of K3 inhibition (Figure 3A), which suggests PKR variants
251 did not often substantially modulate inherent properties of PKR, like its expression.

252 We found PKR variants that were not tolerated, though perhaps fewer than we would
253 expect given the kinase domain is responsible for carrying out its critical function. These came
254 in two flavors: variants that increased susceptibility to K3, and variants that were deleterious for
255 PKR function. We were surprised to find sites enriched for K3-susceptible variants, such as
256 Phe278, Arg453, and Ser492. These could be sites where the wild-type residues help
257 discriminate between eIF2α and K3. These sites do not cluster together; however, when
258 projected onto the surface of PKR they appear to be intermingled with essential residues
259 (Figure 6A). This could suggest that while they are not needed to recognize eIF2α in normal
260 conditions, they are well-positioned to discriminate between eIF2α and a pseudosubstrate
261 inhibitor. Finally, the correlation of PKR functional scores between K3 and K3-H47R suggests
262 resistant variants are resilient. This agrees with prior work screening a few PKR variants against
263 vaccinia K3-H47R and the K3 homolog from variola virus (13). We would be curious to know if
264 this pattern holds for more highly diverged K3 orthologs (29) and other pseudosubstrate
265 inhibitors, such as Ranavirus vIF2α (30).

266 The genetic pliability observed in the PKR kinase domain is reminiscent of that seen with
267 another innate immunity factor, TRIM5α, which is locked in an evolutionary arms race with
268 retroviral capsids (31,32). Both PKR and TRIM5α have access to “rolling hills" of resistant
269 variants (Figure 6B), in opposition to sharp cliffs that are highly optimized (32). Notably, unlike
270 PKR, TRIM5α does not have to balance pathogen conflict with enzymatic function. We also note
271 the structural context in which we identified K3-resistant sites, with many being found within
272 secondary structures (e.g. Glu375, Il378, and Glu379 in helix αD, and Glu490, Lys493, and
273 Thr491 in helix αG), whereas in TRIM5α, as well as the immune proteins MxA and NLRP1
274 (33,34), positively selected sites and improved variants have been described in structurally
275 flexible loops and linkers. We also considered contrasts between PKR and ACE2, a host
276 enzyme with sites under positive selection likely due to being targeted by coronaviruses for cell
277 entry (35–37). However, the ACE2 sites under positive selection are not located near the
278 catalytic domain of the enzyme, in contrast to PKR (38–40). Ultimately, it appears that the
279 resolution of this conundrum is that PKR maintains pliability in this region despite its criticality.
280 This pliability is likely made possible by the flexibility of eIF2α’s Ser51 loop in which the
281 phosphorylation site resides; indeed, the loop is unstructured in the co-crystal of PKR and eIF2α
282 (5). As such, while we still don’t have a clear picture of what phosphorylation of eIF2α looks like,
283 we can appreciate the flexible nature of eIF2α during its interaction with PKR (5,14,24,28).
284 Further biochemical and structural investigation will be necessary to interrogate the ability of
285 variants in PKR to disrupt interactions with K3 while maintaining eIF2α targeting. We note that
286 while we were able to identify many sites of interest across the PKR kinase domain, variation at
287 many other sites in PKR remains to be explored and may harbor allosteric effects on
288 pseudosubstrate resistance.
289 Barring possible variation in under-studied populations, there is little allelic diversity of
290 PKR in the human population, with all nonsynonymous variation listed as rare in gnomAD (41).
291 PKR does exhibit sequence diversity in comparisons across species, including primates (14,42).

292 We expect viruses could exert selective pressure on rare heterozygous variation in PKR, as we
293 would expect beneficial variants in PKR that evade pseudosubstrate inhibitors to be dominant,
294 given that a small amount of eIF2α phosphorylation is capable of halting protein synthesis (43).
295 We found an enrichment for vaccinia K3-resistant variants at sites previously found to be
296 under positive selection (13,14). In effect, these are two independent approaches that both
297 pinpoint these sites as genetically pliable: positive selection analysis retrospectively considers
298 existing variation in nature across multiple homologs, whereas deep mutational scanning
299 prospectively tests novel variants in a single homolog. We and others (32,33) view deep
300 mutational scanning experiments as a complementary approach to positive selection analysis.
301 One strength of deep mutational scanning is its potential to illuminate sites of opportunity
302 against pathogens that have not exerted historical evolutionary pressure. It can also allow for
303 the testing of insertions or deletions (44) which are generally discarded in positive selection
304 analysis. On the other hand, a limitation of the deep mutational scanning approach is that it only
305 tests variant function in a limited set of conditions, when the evolutionary selection could be a
306 symphonic signal made up of a myriad of unknown pressures. Deep mutational scanning also
307 requires the function of the protein to be testable in a selectable assay. While proteins with cell-
308 extrinsic or whole-organism phenotypes would be harder to test, recent advances in high-
309 throughput genetic experimentation may allow deep mutational scans of those proteins as well
310 (45,46).
311
312 **IDEAS AND SPECULATION**
313 One might naively expect a PKR pseudosubstrate inhibitor to be a closer mimic of the
314 natural PKR substrate, eIF2α, which would make it more difficult for PKR to distinguish it from
315 eIF2α. One possibility is that K3 pseudosubstrate divergence from eIF2α has been selected to
316 allow the inhibitor to bind PKR with even higher affinity than eIF2α does. But mutations that
317 improve binding to one species' PKR homolog might decrease binding to the divergent PKR

318 homologs from other species (47–49). Thus, pseudosubstrate inhibitors of generalist poxviruses
319 may need to evolutionarily balance improving PKR binding for one host against maintaining
320 PKR binding of multiple hosts. Interestingly, the structural component most diverged between
321 K3 and eIF2α, a rigid helix in K3 in place of eIF2α's flexible phospho-acceptor site, primarily
322 interacts with the residues around the activation loop of PKR (Figure 6C), which we found to be
323 highly functionally constrained. In contrast, amino acids 72-83 of K3 are highly identical to eIF2α
324 and interact primarily with PKR's divergent helix αG (Supplemental Figure 6). Thus, vaccinia K3
325 may well have been evolutionarily constrained to avoid limiting host range. While the host range
326 of vaccinia is not fully understood (50), current evidence suggests vaccinia is a generalist
327 (29,48). Poxviruses as a whole infect a very wide range of species, which suggests the
328 ancestral K3 needed to be compatible with a wide host range.

329 Despite its pliability, PKR helix αG is believed to play a critical role in eIF2α binding and
330 phosphorylation, as it induces a conformational shift in eIF2α that moves the Ser51 phospho-
331 acceptor site into PKR's ATP-binding site. Based on our findings and positive selection
332 analyses, this conformational shift is apparently amenable to variation in the PKR kinase
333 domain. Perhaps the resilience of the binding surface between PKR and eIF2α could be
334 informative for the budding field of de novo protein design, as resilient design is a critical
335 consideration for vaccines and therapeutics faced with rapidly evolving infections agents.

336 **MATERIALS AND METHODS**

337 **PKR and K3 plasmid construction**

338 We generated the plasmid MSp508_MCS as the base plasmid for all experiments by
339 inserting a multiple-cloning site (MCS) into the single-copy plasmid YCp50, a gift from Mark
340 Rose (51). The MCS contained seven unique restriction enzyme cut sites: AgeI, BsiWI, BstEII,
341 NotI, MluI, PvuII, and SacI. YCp50 was digested using restriction enzymes EcoRI-HF (NEB
342 Cat#R3101S) and BspDI (NEB Cat#R0557S) with rCutSmart buffer, followed by purification and
343 size selection on a 1% agarose gel with 0.6 µg/mL ethidium bromide (BioRad Cat#1610433),
344 selecting for the 7,961 bp band. The extracted band was purified using a QIAquick Gel
345 Extraction kit (Qiagen Cat#28706) and eluted with 30 µL of water. For Gibson Assembly the
346 purified band was combined with a single-stranded DNA oligonucleotide containing the MSC
347 and homology arms spanning the digest site, named Oligo 1 (Supplemental File), in a 1:5 molar
348 ratio in a total volume of 5 µL, along with an additional 5 µL 2x Gibson Assembly Master Mix
349 (NEB Cat#E2611L). The reaction mixture was incubated at 50°C for 1 hour. One microliter of
350 the Gibson Assembly reaction was transformed into 10 µL 5-alpha competent E. coli (NEB
351 Cat#C2987I) and plated onto 10-cm LB-AMP plates (IPM Scientific Cat#11006-016) and
352 incubated overnight at 37°C. Colonies were selected for overnight outgrowth in 3 mL LB-AMP
353 (IPM Scientific Cat#11006-004), followed by a QIAprep spin miniprep (Qiagen Cat#27106) and
354 Sanger sequencing to validate the plasmid sequence using the primer Oligo 2. This produced
355 the plasmid MSp508_MCS.

356 We cloned wild-type PKR, wild-type K3, and K3-H47R into the MCS of MSp508_MCS to
357 produce the MSp509_PKR-WT, MSp510_K3-WT, and MSp511_K3-H47R plasmids,
358 respectively. The plasmid p1419 (23) contains the *PKR* gene (standard name *EIF2AK2)* under
359 the control of the galactose-inducible pGAL10/CYC1 promoter for yeast expression. We PCR-
360 amplified the PKR expression construct using primers (Oligos 3 and 4) to place pGAL10/CYC1-
361 *PKR* on MSp508_MCS between AgeI and BstEII. Oligo 4 incorporated a synthetic terminator for

362 *PKR*, T_{synth1} (52), a 28-bp spacer sequence, and a 26-bp barcode
363 (CGCTTAATATGCAATGAAATTGCTTA); the primers added 20-bp homology arms for cloning
364 onto the MSp508_MCS plasmid. PCR was performed using the polymerase PfuUltraII (Agilent
365 Technologies Cat#600674) for 30 cycles with an annealing temperature of 55°C, followed by gel
366 purification. MSp508_MCS was digested with restriction enzymes AgeI-HF (NEB Cat#R3552S)
367 and BstEII-HF (NEB Cat#R3162S), followed by gel purification. The digested MSp508_MCS
368 and pGAL10/CYC1-PKR fragments were joined via Gibson Assembly in a 1:5 molar ratio,
369 followed by transformation into 5-alpha competent *E. coli* and plating onto LB-AMP. A resultant
370 clone, validated by Sanger sequencing, was designated MSp509_PKR-WT.
371 To produce MSp510_K3-WT, the *K3L* coding sequence was amplified from the plasmid
372 pC140 (23) using primers Oligo 5 and Oligo 6. Similarly, to produce MSp511_K3-H47R, the
373 *K3L-H47R* coding sequence was amplified from the plasmid pC407 using primers Oligo 6 and
374 Oligo 7. pC140 and pC407 were gifts from Thomas Dever. We note that the *K3L* alleles on
375 these plasmids carry a Val2Leu mutation relative to the VACV-WR *K3L* (Genbank
376 AAO89313.1), which was introduced during the cloning of *K3L* on the original plasmid pTM1
377 (19). Oligos 5 and 7 incorporated a synthetic terminator (T_{synth8}) for the K3 allele (52), a 28-bp
378 nucleotide spacer sequence, a 26-bp barcode (ATCGTAATAGGTTTCCGGCTTGTTCG and
379 ACAGGAAATGCTTTCGGGGTTGTATT, respectively), and a 20-bp homology arm to
380 MSp508_MCS. The pTDH3 promoter, also known as pGPD, was amplified from genomic DNA
381 of the yeast strain BY4742 (53) using primers Oligo 8 and Oligo 9). K3-WT, K3-H47R, and
382 pTDH3 were amplified using PfuUltraII, followed by gel purification. MSp508_MCS was digested
383 with restriction enzymes NotI-HF (NEB Cat#R3189S) and PvuII-HF (NEB Cat#R3151S). Each
384 K3 allele (K3-WT and K3-H47R) was joined with a pTDH3 promoter onto the digested
385 MSp508_MCS via Gibson Assembly in a 1:5:5 molar ratio, followed by transformation into 5-
386 alpha competent *E. coli* and plating onto LB-AMP. Resultant clones, validated by Sanger
387 sequencing, were designated as MSp510_K3-WT and MSp511_K3-H47R.

388 MSp512_K3Δ58 was made by removing nucleotides 1-173 of the *K3L* sequence of
389 YCp50_K3, leaving codons 59-88 to generate a nonfunctional *K3L* allele (denoted K3Δ58)
390 under the pTDH3 promoter. The K3Δ58 sequence was amplified from the MSp510_K3-WT
391 plasmid using primers Oligo 10 and Oligo 11. MSp510_K3-WT was digested with restriction
392 enzymes NotI-HF and MluI-HF (NEB Cat#R3198S), followed by gel purification and size
393 selection for the 8,684 bp band. The K3Δ58 allele was joined with the MSp508_MCS digested
394 fragment via Gibson Assembly in a 1:5 molar ratio, followed by transformation into 5-alpha
395 competent E. coli and plating onto LB-AMP. A resultant clone was validated by Sanger
396 sequencing and designated as MSp512_K3Δ58.
397
398 **Generation of the *PKR* variant library**
399 We made the *PKR* variant library by 15 Gibson Assembly reactions using pairs of PCR
400 amplicons targeting 4 windows of PKR protein sequence: 255-278 (5 pairs of reactions), 371-
401 385 (3 pairs of reactions), 448-455 (2 pairs of reactions), and 480-506 (5 pairs of reactions). In
402 each pair, one of the PCR reactions, PCR-1, utilized a pool of forward primers, termed a variant
403 primer tile set, containing single-base deviations from the *PKR* sequence to generate all SNP-
404 accessible variants in a stretch of X to Y consecutive codons (Supplemental Figure 9). Each
405 forward primer in a tile set was composed of a 20-bp homology arm, the variant region, and a
406 priming region with a melting temperature of 50°C. The reverse primer of all PCR-1 reactions
407 had a constant 20-bp homology arm, a barcode region with 20 fully mixed bases, and a
408 constant PCR-priming region homologous to the end of *PKR* with a melting temperature of 55°C
409 (Supplemental Figure 10). Mixed bases in the barcodes were limited to 5-nucleotide stretches to
410 prevent the unintended generation of restriction sites, spacing these stretches with “AA” or “TT”
411 sequences (54). The forward PCR-1 primer tile sets are listed in the Supplemental File as
412 Oligos 12-26, and the reverse PCR-1 barcode primer is listed as Oligo 27. The paired PCR-2
413 reaction was an inverse PCR that generated the remainder of the *PKR* gene and plasmid

414 backbone, with overlaps to the homology arms of PCR-1; the forward primer for PCR-2
415 reactions was Oligo 28, and the reverse primers were Oligos 29-43. Thus, Gibson Assembly of
416 these PCR products would generate sets of *PKR* variants in defined segments of *PKR* along
417 with random barcodes at the end of the gene (Supplemental Figure 11).
418 We used custom Python (v3.8.18) scripts to design each variant-introducing primer,
419 utilizing IUPAC degenerate base symbols (e.g. “D” represents a mix of “A”, “G”, and “T”)
420 (55,56). The introduced variant amino acids were all within a single base change from the
421 canonical human *PKR* coding sequence (Genbank M85294.1:31-1686); we note the *PKR*
422 sequence encoded on MSp509_PKR-WT differs somewhat from the canonical sequence
423 through synonymous substitutions. Primers were synthesized by Integrated DNA Technologies,
424 then were pooled manually into variant primer tiles sets.
425 PCR-1 reactions were amplified from the MSp509_PKR-WT plasmid using PfuUltraII
426 polymerase with an annealing temperature of 45°C. Each reaction generated a pool of *PKR*
427 gene fragments containing a single nonsynonymous variant paired with a unique barcode
428 sequence. In parallel, PCR-2 reactions amplified vector fragments from MSp509_PKR-WT
429 plasmid using Herculase II polymerase (Agilent Technologies Cat#600677) using cycling
430 conditions for vector targets >10 kb. PCR-1 and PCR-2 amplicons were digested with DpnI
431 (NEB Cat#R0176S) for 2 hours at 37°C to remove the MSp509_PKR-WT template DNA,
432 followed by gel purification. Each PCR-1 amplicon was paired with its corresponding PCR-2
433 amplicon for Gibson Assembly in a 1:5 molar ratio.
434 Two µL of each Gibson Assembly was transformed into 50 µL of 5-alpha competent *E.*
435 *coli* and all cells were plated on LB-AMP and incubated overnight at 37°C. Colonies were
436 counted on each plate and plates were bottlenecked at approximately 30 colonies per selected
437 nonsynonymous variant (i.e. each nonsynonymous variant would be linked to approximately 30
438 unique barcode sequences). Plates were washed with 15 mL LB-AMP, cell densities were
439 measured as the optical density at 600 nm (OD_{600}), and an equal number of cells (approximately

440 5 × 10^9 cells) from each reaction were pooled to form a single *PKR* variant library. A 200 mL LB-
441 AMP outgrowth was grown to an OD_{600} measurement of approximately 3, followed by a Qiagen
442 MAXI plasmid prep (Qiagen Cat#12963).
443
444 **PacBio sequencing of barcoded variant libraries**
445 The *PKR* variant library was sequenced using the PacBio Sequel II instrument to identify
446 the barcodes that were linked to each nonsynonymous variant. Sixteen micrograms of the *PKR*
447 variant library were digested with restriction enzymes AgeI-HF and NotI-HF to create linear
448 fragments of approximately 2,100 bp for sequencing. The digest was incubated for 2 hours at
449 37°C then purified using a QiaQuick PCR purification kit (Qiagen Cat#28106). Fragments of
450 2,100 bp were size-selected using a SageELF instrument (Sage Science) before PacBio circular
451 consensus sequencing (CCS) HiFi sequencing on a Sequel II instrument (Pacific Biosciences).
452 From the CCS reads we generated a table of *PKR* barcodes paired with genetic variants using
453 alignparse v0.2.6 and custom Python scripts (57).
454
455 **Combining *PKR* variant library with K3 alleles**
456 We next cloned the three K3 alleles (K3, K3-H47R, and K3Δ58) onto the PKR variant
457 library plasmids. The PKR variant library was digested with NotI-HF and PvuII-HF to generate a
458 10,270 bp receiver DNA fragment, while the K3 alleles were separately digested with BstEII-HF
459 and SacI-HF (NEB Cat#R3156S) to generate a 1,130 bp insert DNA fragment with 20-bp
460 homology arms with homology to the receiver fragment for Gibson Assembly. For each of the
461 reactions, 10 µg of plasmid DNA was digested with 5 µL of each restriction enzyme in a 50 µL
462 reaction to generate a linear fragment, followed by gel purification. The PKR and K3 fragments
463 were combined in three separate Gibson Assembly reactions in a 1:5 molar ratio with 100 ng of
464 the PKR vector fragment in a reaction volume of 20 µL and incubated at 50°C for 1 hour. A

465 standard ethanol precipitation was performed on each reaction, adding 100 µL of 100% ETOH
466 and incubating overnight at -20°C before resuspending the pellets in 2 µL of water (58).
467 We transformed each of the three concentrated reactions into *E. cloni* 10G SUPREME
468 electrocompetent cells (Lucigen Cat#60080-2) using a MicroPulser Electroporator (BioRad),
469 with 2 µL of the concentrated reaction combined with 25 µL of competent cells. Following the
470 electroporation and recovery, cells were plated onto two 15-cm LB-AMP plates. A 1:1000
471 dilution was plated with 100 µL of water on a 10-cm plate to estimate the number of transformed
472 colonies across the two 15-cm plates, which produced an estimate of approximately 2 million
473 colonies per electroporation. Plates were washed with 25 mL LB-AMP, combining the two plates
474 for each of the reactions. Each library was expanded in 200 mL LB-AMP to an OD_{600}
475 measurement of approximately 3, followed by a Qiagen MAXI plasmid prep.
476
477 **Screening the PKR-K3 variant pairs in a yeast growth assay**
478 All yeast growth was at 30°C in CSM-Ura (Sunrise Science Products Cat#1004-010),
479 and liquid cultures were shaken at 200 revolutions per minute. We transformed each of the
480 three paired libraries (PKR + K3, PKR + K3Δ58, and PKR + K3-H47R) into yeast in duplicate.
481 The paired plasmid libraries were transformed into the yeast strain BY4742 (*MAT*α *ura3*Δ0
482 *leu2*Δ0 *his3*Δ1 *lys2*Δ0; strain name MSY2) (53) using a standard large-scale high efficiency
483 lithium acetate transformation protocol (59) and plated onto 15-cm plates with 2% dextrose,
484 using 1:1,000 and 1:10,000 dilutions on 10-cm plates to estimate colony counts, which
485 produced approximately 100,000 colonies. Colonies were washed off plates with 25 mL media
486 with 2% dextrose.
487 To start the yeast growth assay, six cultures were seeded at low density (OD_{600}
488 measurement of 0.01) in 40 mL media with 2% dextrose and grown overnight for 16 hours. The
489 following morning cultures were moved from 30°C to 4°C to pause growth, then restarted at an
490 OD_{600} of 0.25 in 40 mL media with 2% dextrose 3 hours prior to GAL induction. After 3 hours,

491 once all cultures were in a log growth phase, approximately 1×10^8 cells were taken from each
492 culture as the starting timepoint sample (designated as “0 hours”). All timepoint samples were
493 spun down in a 1.5 mL Eppendorf tube at 5,000 rpm for 1 minute, after which supernatant was
494 removed and the pellet was frozen at -80°C. Approximately 2×10^8 cells from the remaining
495 cultures were pelleted in 50 mL conical tubes at 3,000 rpm, supernatant was removed, and cells
496 were resuspended in 80 mL CSM-Ura media with 2% galactose (OD_{600} measurement of 0.125
497 OD_{600}) to induce PKR expression. Cultures were incubated overnight at 30°C, 200 rpm.
498 Additional samples were harvested at 12, 16, and 20 hours post-PKR induction, with
499 approximately 1×10^8 cells taken at each timepoint. The culture density was monitored and
500 back diluted to maintain a log growth phase (OD_{600} measurement less than 1). With three K3
501 allele conditions (K3, K3Δ58, and K3-H47R), four timepoints (0, 12, 16, and 20 hours) and two
502 replicates, a total of 24 samples were taken across the yeast growth assay.
503

504 **Plasmid extraction and barcode amplification**

505 To quantify changes in barcode abundance between timepoints in the yeast growth
506 assay, we harvested plasmids from the four timepoints for each K3 allele, then amplified and
507 sequenced the adjacent PKR and K3 barcodes in each plasmid. Plasmids were harvested from
508 the yeast samples using a modified QIAprep spin miniprep protocol (60). Sampled cell pellets
509 were first thawed at room temperature, followed by the addition of 250 µL QIAprep P1 buffer
510 and 2 µL zymolyase (2.5 units per µL), and incubation at 37°C for 30 minutes, followed by
511 adding 250 µL P2 buffer and following the manufacturer instructions for the remainder of the
512 protocol.

513 To identify and quantify the abundance of each PKR variant paired with each of the
514 three K3 alleles we performed Illumina sequencing of the PKR barcodes from the plasmids. We
515 used a two-step PCR protocol, the first to amplify the PKR barcode from the plasmids and the
516 second to attach Illumina adapters and Nextera indices for downstream sequencing and sample

517 demultiplexing. For the first PCR reaction, we designed forward and reverse primers as a pool
518 of five primers each, that had 0 to 4 “N” bases between the Nextera transposase adapter
519 sequence and the priming sequence to stagger the base signal per cycle and maintain
520 sequence diversity across the flow cell (61). The forward primers (Oligos 44-48) with a melting
521 temperature of 60°C were pooled together and used for all PCR-1 reactions, annealing
522 immediately upstream of the PKR barcode locus. Five reverse primers were designed and
523 pooled for amplification from each of the three K3 alleles that annealed within the three distinct
524 K3 barcode sequences (Oligos 49-53 for K3, Oligos 54-58 for K3Δ58, and Oligos 59-63 for K3-
525 H47R). One microliter of each primer pool was combined with 50 ng of sample plasmid DNA
526 and 25 µL Kapa Hifi Hotstart ReadyMix (Kapa Biosystems Cat# KK2602), and topped off to a
527 total volume of 50 µL with water. PCR cycling was performed as follows: (1) 95°C for 3 minutes,
528 (2) 98°C for 20 seconds, (3) 65°C for 15 seconds, (4) 72°C for 1 minute, repeat steps 2-4 for a
529 total of 18 cycles, (5) 72°C for 1 minute, (6) 12°C hold. PCR products were purified using a
530 MinElute PCR purification kit (Qiagen Cat#28006) using 11 µL water for the final elution, then
531 quantified using a Qubit dsDNA High Sensitivity (HS) kit (ThermoFisher Scientific Cat#Q32851).
532 For the second PCR reaction, 10 ng of amplicon DNA from the first PCR reaction was
533 combined with 10 µL of Nextera adapter index primers (Illumina Cat#20027213) and 25 µL
534 Kapa HiFi Hotstart ReadyMix, and topped off to a total volume of 50 µL with water. PCR cycling
535 was performed as follows: (1) 100°C for 45 seconds, (2) 100°C for 15 seconds, (3) 60°C for 30
536 seconds, (4) 72°C for 30 seconds, repeat steps 2-4 for a total of 8 cycles, (5) 72°C for 1 minute,
537 (5) 12°C hold. PCR products were purified using a MinElute PCR purification kit using 11 µL of
538 water for the final elution, then quantified using a Qubit dsDNA Broad Range (BR) kit
539 (ThermoFisher Scientific Cat#Q32850). 500 ng of the second PCR reaction amplicons were gel
540 purified on a Size Select II E-Gel (ThermoFisher Scientific Cat#G661012) for approximately 13
541 minutes to extract the approximately 250-bp amplicon band, followed by quantification with a
542 Qubit dsDNA HS kit. Amplicon samples were diluted to 4 nM before being pooled together,

543 followed by manufacture denature and dilution protocols (Illumina Document#15039740v10)
544 before sequencing on an Illumina NextSeq 2000 instrument.
545
546 **PKR functional scores and screening analysis**
547 Next, we extracted PKR barcode sequences from the Illumina reads and mapped the
548 barcodes back to their corresponding select nonsynonymous variants using the table of PKR
549 barcodes paired with genetic variants generated from the PacBio CCS HiFi reads. Paired reads
550 were assembled into contiguous sequences using PEAR v0.9.11 (62), followed by Bartender
551 v1.1 (63) to extract and cluster PKR barcodes using the barcode search pattern "CAAGG[25-
552 27]GGTGA".
553 We wrote Python v3.8.18 scripts to tally the PKR barcodes and map them back to
554 genetic variants using the table generated from the PacBio CCS HiFi reads. Barcode counts
555 were normalized to the total read count for each of the four timepoints across each of the K3
556 alleles, followed by a fold change calculation for each PKR barcode across timepoints 0, 12, 16,
557 and 20 hours:
558 $$FC_{TP} = -log_2(\frac{Normalized\ Reads_{TP}}{Normalized\ Reads_0})$$
559 where FC_{TP} is the fold change in normalized reads for a PKR barcode from 0 hours to a
560 subsequent timepoint (TP), $Normalized\ Reads_{TP}$ is the read count for a given barcode divided
561 by the total number of reads at the given timepoint, and $Normalized\ Reads_0$ is the read count for
562 a given barcode divided by the total number of reads at the 0-hour timepoint. Of note, the $\log_2$ of
563 the fold change is inverted such that functional PKR variants that inhibit yeast growth and
564 decreased in abundance were assigned positive fold change value. We then calculated PKR
565 functional scores for each PKR barcode in each of the K3 alleles by calculating the area under
566 the curve using the composite trapezoidal rule. We calculated the PKR functional score for each
567 variant for each K3 allele by averaging the PKR functional score across all representative

568 barcodes for a given variant. As we found a strong correlation between replicates (Pearson
569 correlation coefficient > 0.98 for each K3 allele, Supplemental Figure 3), we proceeded by
570 combining all reads from the two replicate experiments for each K3 allele and recalculating the
571 fold changes and PKR functional scores for each barcode as described above.
572
573 **Predicted PKR complexes and substrate contacts**
574 All molecular graphics and analyses were performed using USCF ChimeraX v1.5 and
575 PyMol v2.5.4. To define PKR residues contacting K3 and eIF2α we used the AlphaFold2
576 structure prediction tool (ColabFold v1.5.5) in UCSF ChimeraX v1.5 (64,65) (Supplemental
577 Figure 12A). We aligned these predictions to existing crystal structures (PDB 2A1A and 1LUZ)
578 and found the AlphaFold2 predictions to largely represent the crystal structures (RMSD < 1
579 angstrom for both alignments, Supplemental Figure 12B-D) (5,22). We note the low confidence
580 score (pLDDT < 50) of the eIF2α flexible loop containing Ser51, which adopts a compact helical
581 conformation in the predicted model and closely matches the conformation observed in the
582 crystal structure of unbound yeast eIF2α (PDB 1Q46) (66). As Ser51 of eIF2α would need to
583 travel approximately 17 Å to reach PKR's active site (5), this predicted structure is likely
584 reflective of a pre-phosphorylation complex, and thus would not capture contacts between PKR
585 and eIF2α made during phosphorylation. The corresponding loop is unresolved in the crystal
586 structure of human PKR in complex with eIF2α (PDB 2A1A). Note that we opted not to use the
587 existing structure for defining contact residues, both for consistency with the K3 contact
588 definitions, as there is no PKR-K3 co-crystal, as well as for the potential to capture interactions
589 mediated by residues unresolved in the crystal structure (PDB 2A1A, PKR Asp338-Asn350 and
590 eIF2α Glu49-Lys60).
591 To identify potential PKR contact sites from the predicted complex structures, we used
592 PyMol v2.5.4 to select all PKR residue branches within 5 Å of K3 or eIF2α using the command:
593 "sele contacts, br. /{pdb file name}//A within 5 of /{pdb file name}//B" with chain "A" being PKR

and chain “B” being either K3 or eIF2α. Predicted PKR sites that contact K3 were: 275, 276, 278, 304, 339, 343, 345, 375, 379, 382, 414, 416, 435, 448, 449, 450, 451, 452, 453, 455, 460, 485, 486, 487, 488, 489, 490, 492, 493, and 496. Predicted PKR sites that contact eIF2α were: 274, 275, 276, 279, 335, 337, 338, 339, 340, 341, 342, 379, 382, 451, 452, 453, 483, 486, 487, 488, 489, 490, 491, 492, and 493.

PKR sites in the kinase domain under positive selection across vertebrate species were identified by Rothenburg et al. (13): 261, 269-272, 307, 314, 322, 360, 368, 375, 378, 379, 382, 385, 389, 394, 405, 428, 448, 449, 462, 471, 483, 486, 488, 491, 493, 500, 502, 504, 505, 514, 520, and 524. Sites conserved across vertebrate PKR homologs were also identified by Rothenburg et al. (13) which were used for supplementary analysis: 263, 267, 276-279, 281, 283, 296, 298, 308, 309, 312, 315, 317, 319, 320, 323, 327, 362, 364-367, 369, 374, 377, 397, 401, 404, 406, 407, 410-417, 419, 420, 429-433, 437, 444-446, 450, 451, 454, 455, 457-459, 465, 469, 470, 474-477, 480, 490, 511, 519, 523, and 526.

Data access

Supplemental data and code are available under the DOI: 10.5281/zenodo.13788100

ACKNOWLEDGEMENTS

We thank Thomas Dever, Stefan Rothenburg, Adam Phillippy, Bernard Moss, Stephanie Jaquet, Darach Miller, and members of the Sadhu lab for helpful discussions. We thank Thomas Dever and Mark Rose for strains and plasmids. Next-generation sequencing was performed by both the NIH Intramural Sequencing Center (NISC) and the Microarrays and Single-Cell Genomics Core of the National Human Genome Research Institute. This work utilized the computational resources provided by the NIH HPC Biowulf Cluster (http://hpc.nih.gov). This work was supported by the Intramural Research Program of the National Human Genome Research Institute, NIH (1ZIAHG200401).

AUTHOR CONTRIBUTIONS

Designed research/conceptualization: M.J.C. and M.J.S. designed research;

Performed research: M.J.C. and S.B.S. performed research;

Analyzed data: M.J.C., S.B.S., and M.J.S. analyzed data;

Wrote paper: M.J.C. and M.J.S. wrote the paper.

All authors read and revised the paper.

AUTHOR DETAILS

Michael J Chambers

- Center for Genomics and Data Science Research, National Human Genome Research Institute, National Institutes of Health, Bethesda, Maryland, USA
- Department of Microbiology & Immunology, Georgetown University, Washington DC, USA

Contribution: Conceptualization, Investigation, Visualization, Writing - original draft

Competing interests: No competing interests declared

ORCID: 0000-0002-0658-6984

Sophia B Scobell

Center for Genomics and Data Science Research, National Human Genome Research Institute, National Institutes of Health, Bethesda, Maryland, USA

Contribution: Investigation, Analysis, Writing - review and editing

Competing interests: No competing interests declared

ORCID: 0000-0003-4630-0167

Meru J Sadhu

Center for Genomics and Data Science Research, National Human Genome Research Institute, National Institutes of Health, Bethesda, Maryland, USA

Contribution: Conceptualization, Supervision, Analysis, Writing - original draft

For correspondence: meru.sadhu@nih.gov

Competing interests: No competing interests declared

ORCID: 0000-0002-8636-9102

651 **FIGURES**

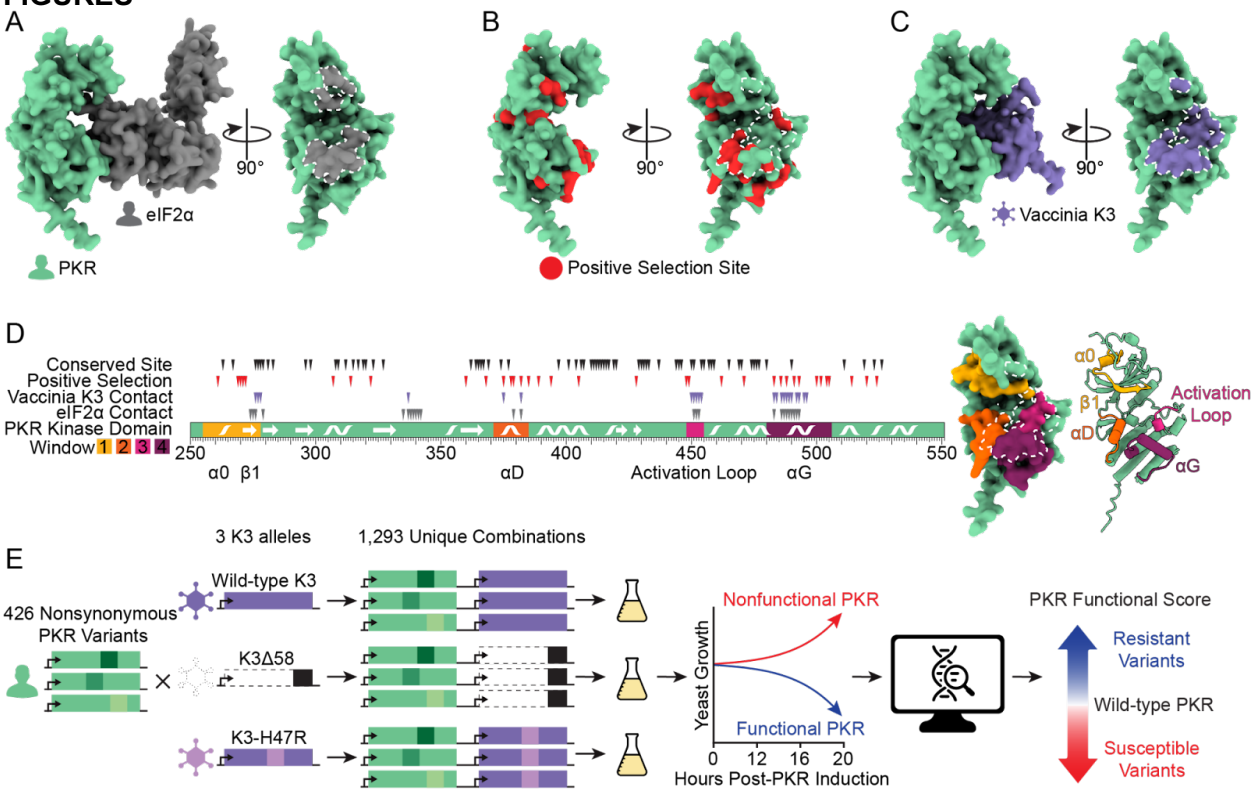

652
653 **Figure 1. Exploring genetic variants of human PKR against the pseudosubstrate**
654 **antagonist vaccinia K3.** (A) (Left) AlphaFold2 model of the PKR kinase domain (green) bound
655 to its target, eIF2α (gray). (Right) Rotated 90°, the eIF2α binding surface of PKR is shaded gray
656 and outlined in white dashed line. (B) PKR kinase domain with vertebrate positive selection sites
657 highlighted in red (13), with the K3 binding surface delineated with white dashed line. (C)
658 AlphaFold2 model of the PKR kinase domain bound to vaccinia K3 (purple). Rotated 90°, the K3
659 binding surface of PKR is shaded purple and outlined in white dashed line. (D) (Left) The PKR
660 kinase domain with four windows highlighted in which we designed 426 nonsynonymous
661 variants. Secondary structures occurring in these windows (alpha helices α0, αD, and αG, beta
662 strand β1, and the kinase activation loop) are marked (5). The positions of conserved sites and
663 sites under positive selection (13) are denoted above with black and red triangles, respectively,
664 and the positions of sites within 5 angstroms of either K3 or eIF2α in an Alphafold2 binding
665 model are denoted with purple and gray triangles, respectively. Note that the modeled
666 interaction between PKR and eIF2α resembles the pre-phosphorylation state in which the
667 phosphoacceptor loop of eIF2α has not entered the PKR active site, and thus there are likely
668 additional sites in PKR that contact eIF2α. (Right) Mutated windows are highlighted on the
669 surface of the PKR kinase domain, with the K3 binding surface delineated with a white dashed
670 line, and in cartoon form with secondary structures marked. (E) Methodological approach to
671 explore the effects of variants of human PKR in the presence of different K3 alleles. 426
672 nonsynonymous variants of PKR were generated and paired with wild-type K3, K3Δ58, and K3-
673 H47R. Variant effects were characterized using a high-throughput yeast growth assay and
674 massively parallel sequencing.

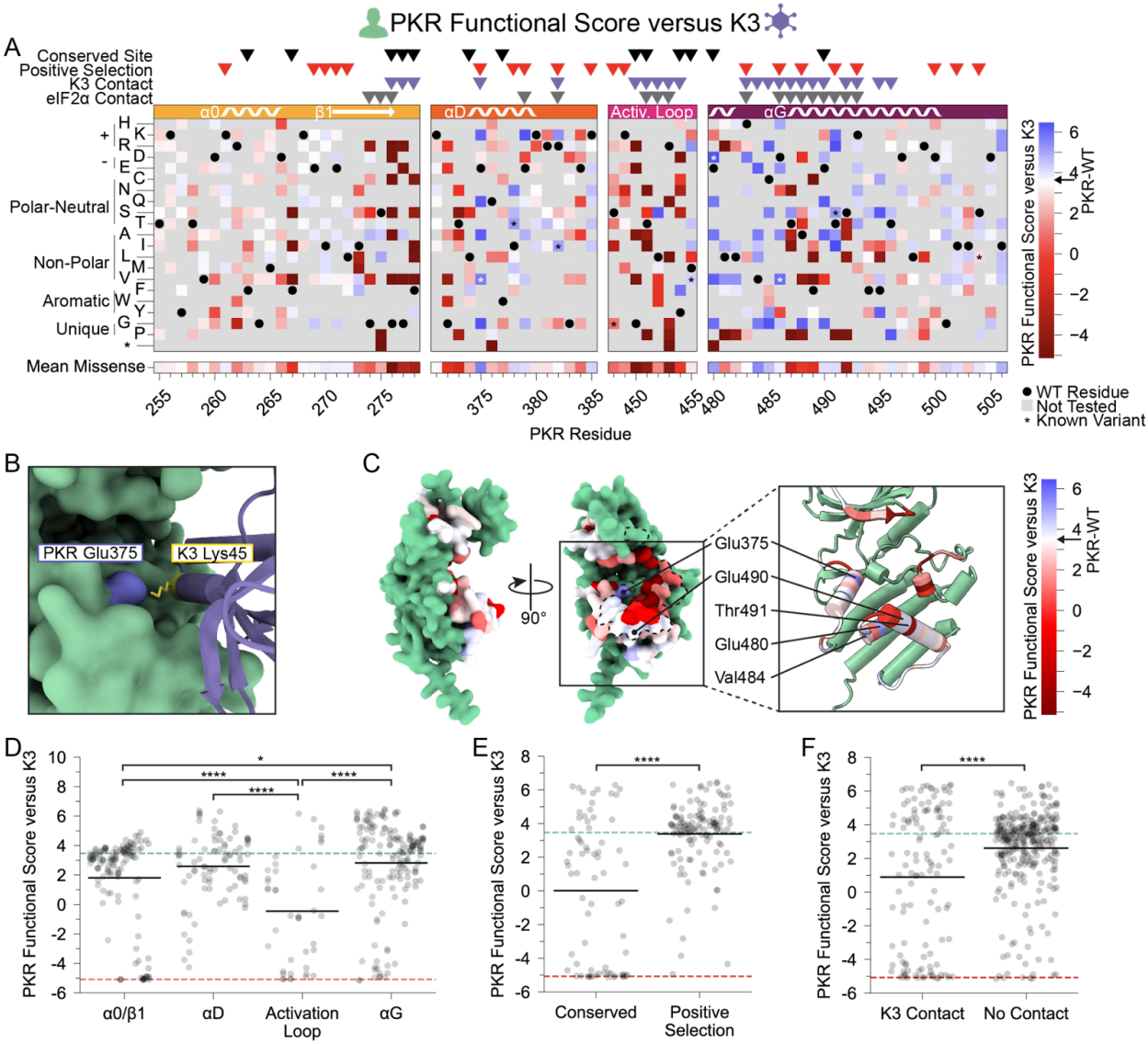

Figure 2. PKR variants that evade K3 and maintain kinase function are enriched at positive selection sites and helices αD and αG. (A-B) PKR functional scores versus K3 are colored ranging from susceptible (red) to WT-like (white) to resistant (blue). (A) Heatmap of PKR variants with cells colored by the PKR functional score versus K3 for SNP-accessible variants. Wild-type PKR residues and untested variants are denoted with black circles and gray squares, respectively. Previously characterized K3-H47R-resistant variants are noted with an asterisk (24). (B) Attractive electrostatic interaction between PKR-Glu375 (blue) and K3-Lys45 (yellow) in the AlphaFold2 model of PKR bound to K3. (C) Surface structure of the PKR kinase domain with sites colored by the mean PKR functional score versus K3 for missense variants. The K3 binding surface is delineated with black dashed line. (Inset) Location of K3-resistant sites cited in the text. (D-F) Strip plots of PKR functional score versus K3 for variants, with green and red dashed lines representing mean scores for WT PKR and nonsense variants, respectively. Variants are partitioned by nearest secondary structural element (D), level of conservation in vertebrates (E), or predicted contact with K3 (F). Points in D are ordered left to right by their position along the kinase domain, whereas they are randomly jittered along the x-axis in E and F. (* $p < .05$, **** $p < .0001$, Tukey's HSD (D) and two-sample t-test (E, F).)

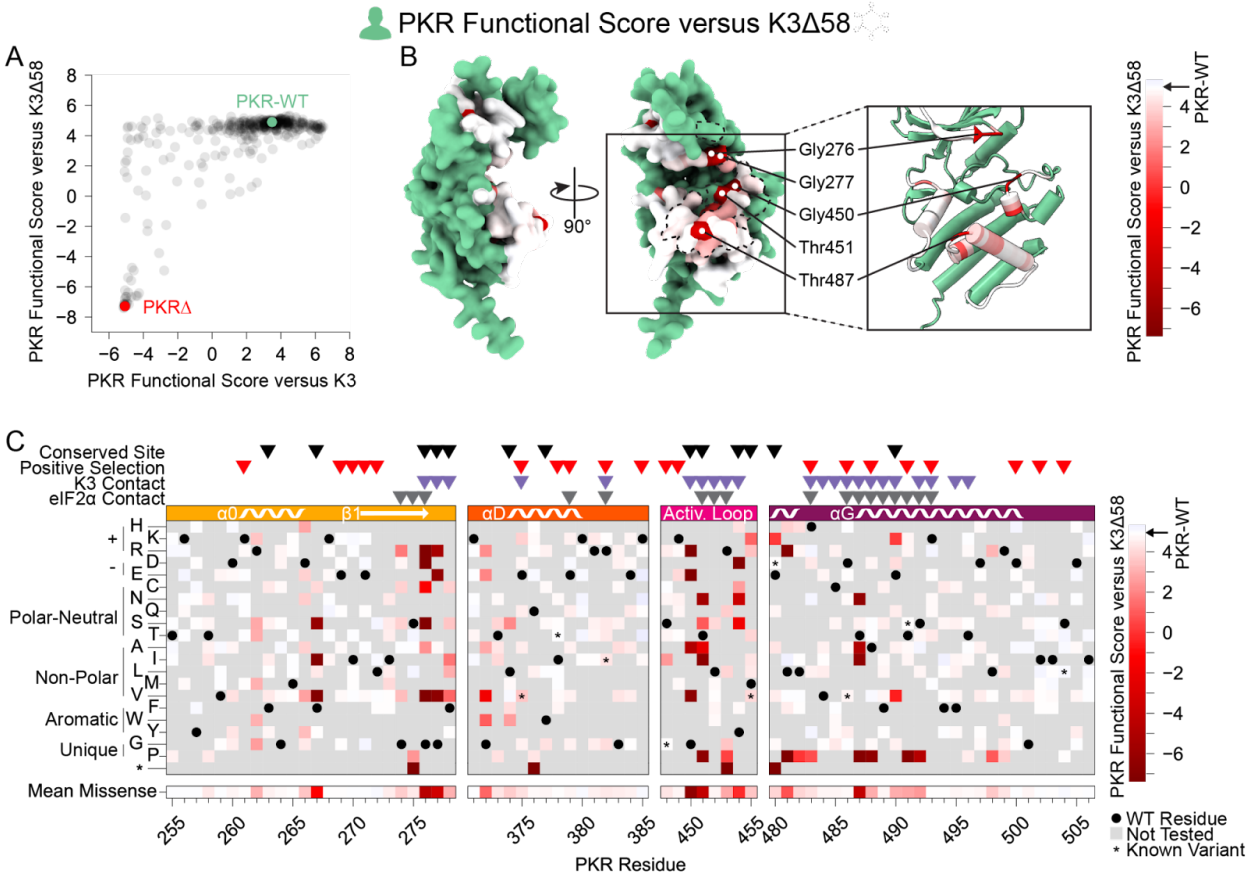

Figure 3. Few nonfunctional PKR variants identified in the absence of K3 inhibition. (A) Scatter plot showing each variant's PKR functional score versus wild-type K3 plotted against its PKR functional score versus K3Δ58. The data point for PKR-WT is colored green and a data point representing the average of the four nonsense variants (PKRΔ) is colored red. (B-C) PKR functional scores versus K3Δ58 are colored ranging from nonfunctional (red) to WT-like (white). (B) Surface structure of the PKR kinase domain with sites colored by the mean PKR functional score versus K3Δ58 for missense variants. The K3 binding surface is delineated with a black dashed line. (Inset) Location of highly constrained sites cited in the text. (C) Heatmap of PKR variants with cells colored by the PKR functional score versus K3Δ58 for each variant.

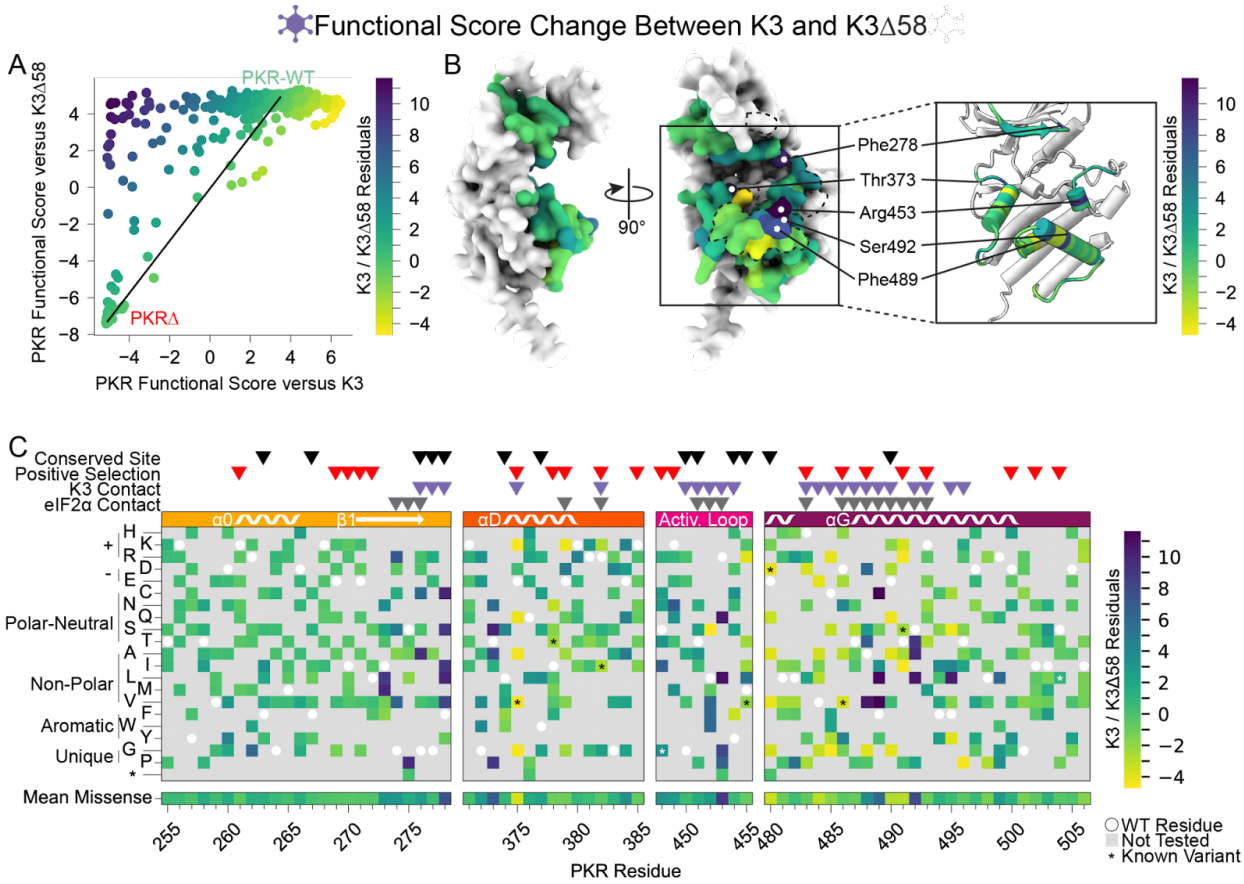

Figure 4. Identification of PKR sites highly susceptible to K3 inhibition. (A) A line was drawn connecting the data point for PKR-WT to the position of the average data point for the four nonsense variants (PKRΔ) from the data in the scatter plot from Figure 3A, with all other data points colored by their residual from that line (K3 / K3Δ58 Residuals), ranging from K3-susceptible (purple) to K3-indifferent (green) to K3-resistant (yellow). This color scheme is used in panels B and C. (B) Surface structure of the PKR kinase domain with sites colored by the mean K3 / K3Δ58 residuals for missense variants. The K3 contact site is delineated with a black dashed line. (Inset) Location of K3-susceptible sites cited in the text. (C) Heatmap of PKR variants with cells colored by the K3 / K3Δ58 residuals for each variant.

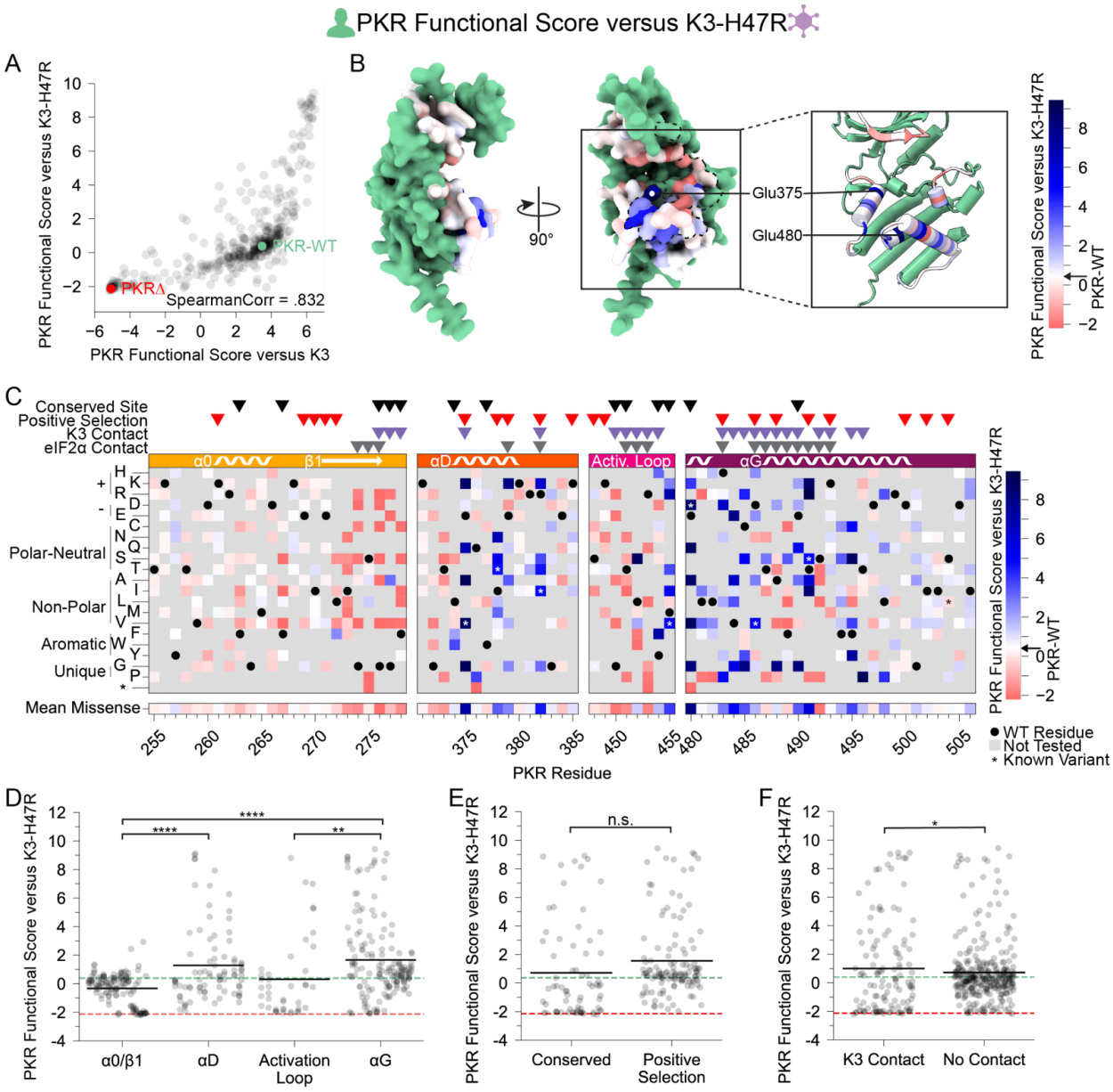

Figure 5. PKR variants that are K3-resistant are also largely K3-H47R-resistant. (A) Scatter plot of PKR functional scores versus wild-type K3 plotted against PKR functional scores versus K3-H47R. The data point for PKR-WT is colored green and a datapoint representing the average of the four nonsense variants (PKRΔ) is colored red. (B-C) PKR functional score versus K3-H47R ranging from susceptible (red) to WT-like (white) to resistant (blue). (B) Surface structure of the PKR kinase domain with sites colored by the mean PKR functional score versus K3-H47R for missense variants. The K3 binding surface is delineated with a black dashed line. (Inset) Location of K3-H47R resistant sites cited in the text. (C) Heatmap of PKR variants with cells colored by the PKR functional score versus K3-H47R for each variant. (D-F) Strip plots of PKR functional scores versus K3-H47R for variants, as plotted in Figure 2D-F. Variants are partitioned by nearest secondary structural element (D), level of conservation in vertebrates (E), or predicted contact with K3 (F). Points in D are ordered left to right by their position along the kinase domain, whereas they are randomly jittered along the x-axis in E and F. (* $p < .05$, ** $p < .01$, **** $p < .0001$, Tukey's HSD (D) and two-sample t-test (E, F).)

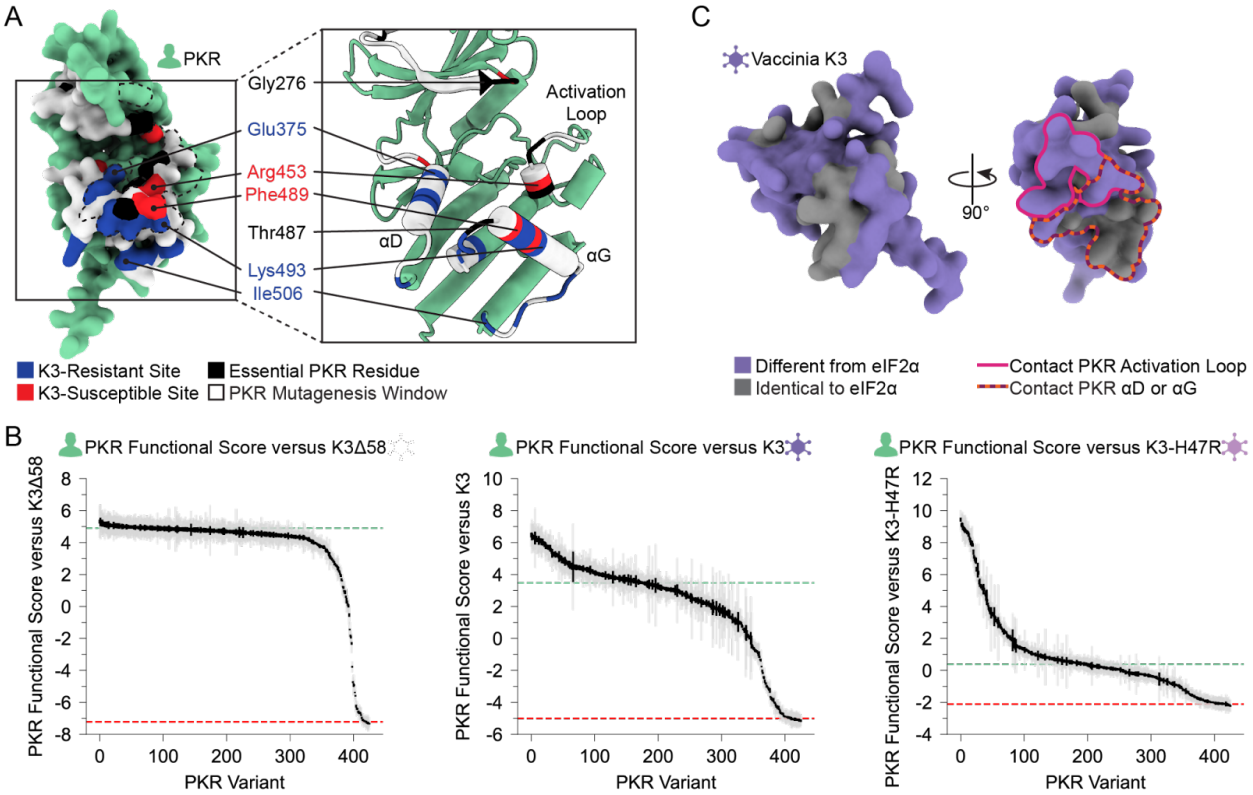

Figure 6. Unified spatial view of highlighted PKR sites across the K3-binding interface. Positions of sites classified as essential residues (black), K3-resistant (blue), and K3-susceptible (red) based upon the above analyses. All other tested sites are marked white. (Left) The vaccinia K3 binding surface of PKR is outlined with a black dashed line. (B) PKR functional scores versus K3Δ58 (Left), K3 (Center), and K3-H47R (Right), with each vertical line representing a PKR variant. Variants are sorted by functional score from high (left) to low (right). Gray and black lines indicate the standard deviation and standard error, respectively, in PKR functional scores across barcodes associated with the given variant. (C) (Left) AlphaFold2 model of Vaccinia K3 with surface residues colored as different from eIF2α (purple) or identical to eIF2α (gray) based on sequence alignment (Supplemental Figure 6). (Right) Rotated 90°, K3 residues that contact the PKR activation loop or helix αD or αG are outlined in pink and dashed orange and burgundy, respectively.

SUPPLEMENTAL FIGURES

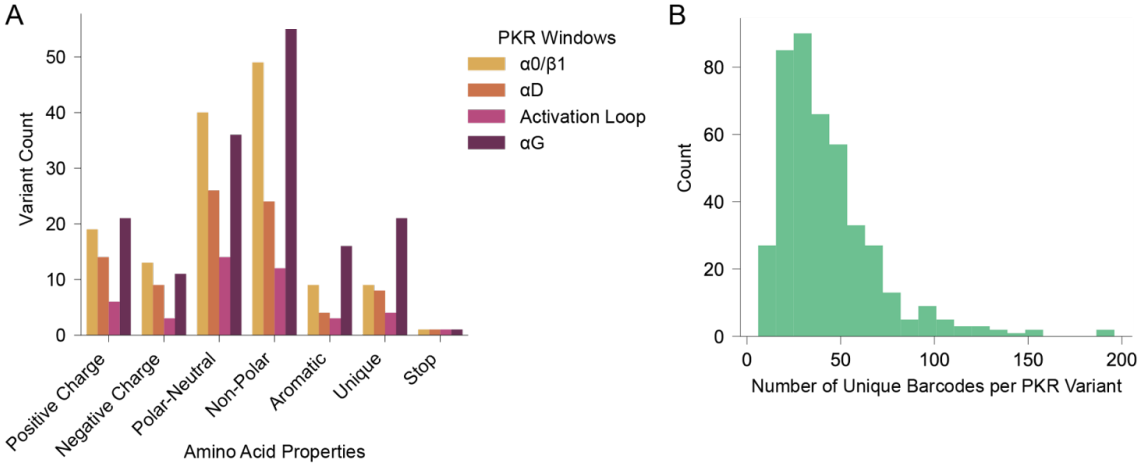

Supplemental Figure 1. Composition of the PKR variant library. (A) Barchart depicts the number of variants made at each of the four PKR windows categorized by amino acid properties: Positive Charge = H, K, R; Negative Charge = D, E; Polar-Neutral = C, N, Q, S, T; Non-Polar = A, I, L, M, V; Aromatic = F, W, Y; Unique = G, P; Stop = *. A total of 140 variants were made in α0/β1, 86 in αD, 43 in the Activation Loop, and 161 in αG for a total of 430 variants, which includes the 4 nonsense variants made in each window. (B) Histogram depicts the number of unique barcodes linked to each PKR variant, with a mean of 42.83.

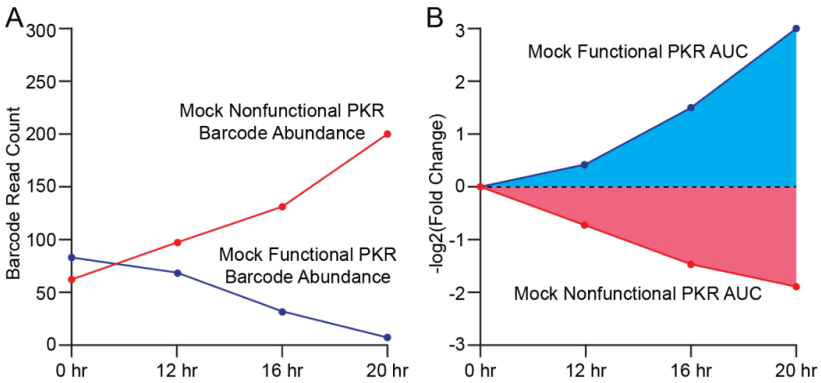

Supplemental Figure 2. Calculation of PKR functional scores from yeast growth assay. (A) Line plot of mock barcode read count data over time for cells expressing nonfunctional (red) or functional (blue) PKR across four sampled timepoints. As PKR activity is toxic to yeast, the number of cells in the pool expressing the functional PKR will decrease over time, and thus the associated barcode read count will also decrease, while the read count for the nonfunctional PKR will increase. (B) Line plot depicting the fold changes from timepoint 0 of barcode abundance derived from Panel A, with a -log2 transformation to assign positive values to functional PKR and negative values to nonfunctional PKR, from which the area under the curve (AUC) is calculated to produce a PKR functional score.

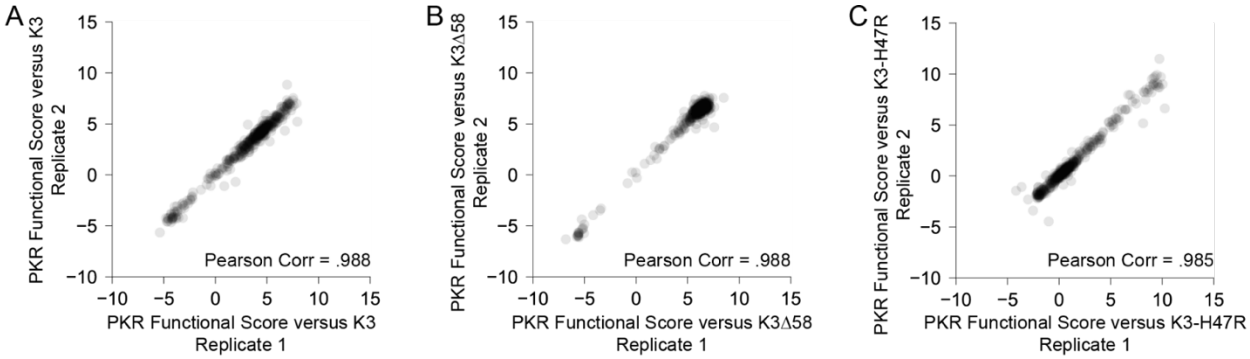

Supplemental Figure 3. Replication of PKR variants paired with K3 alleles. (A) Scatter plot of PKR functional scores for variants paired with K3-WT for two biological replicate experiments. Functional scores were calculated across four timepoints as the area under the curve (see Materials and Methods). Thus, variants with increased evasion of K3 would have higher PKR functional scores, while those with increased susceptibility to K3 or loss of eIF2α kinase activity would have lower scores.

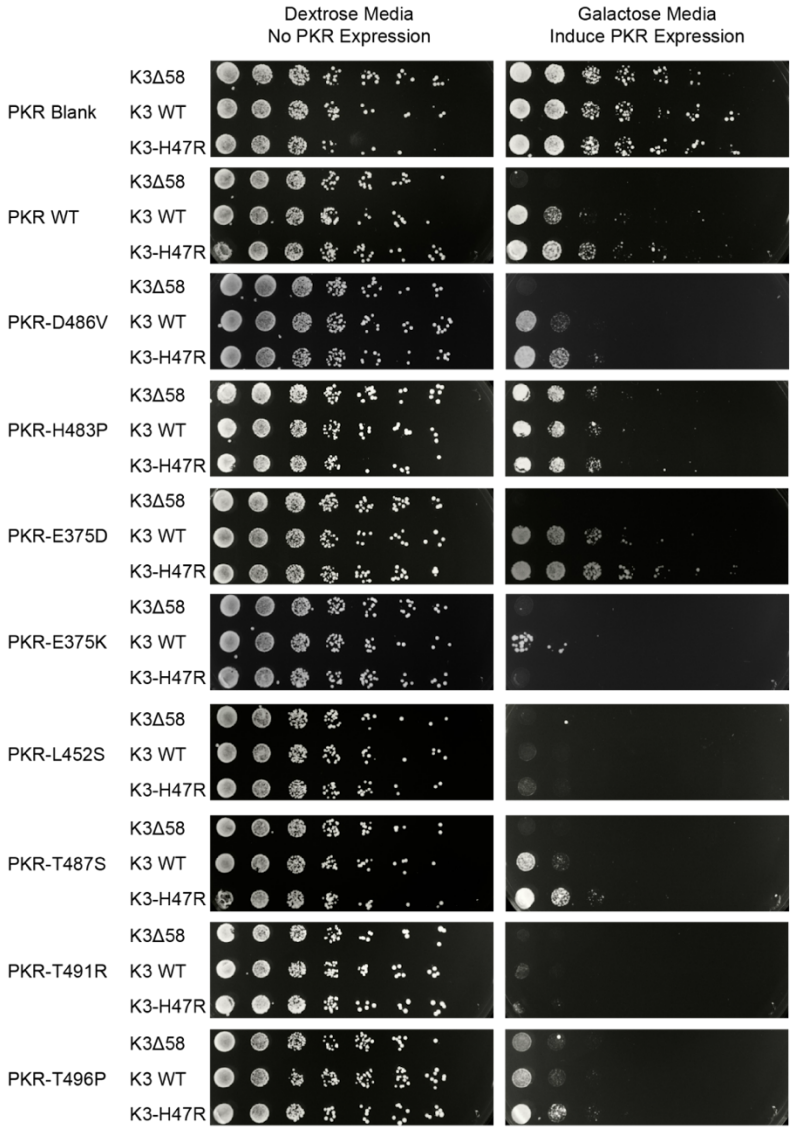

Supplemental Figure 4. Experimental validation of the K3 resistance phenotypes of PKR variants. Select PKR variants were generated and screened against K3Δ58, WT, and H47R alleles using a yeast growth assay visualized through serial dilution (23). PKR is under the inducible pGAL10/CYC1 hybrid promoter, and thus is repressed in dextrose media (left) and expressed in galactose media (right). We selected one variant that exhibited loss of function in the high-throughput screen (H483P, Figure 3C), one variant whose phenotype was similar to PKR WT (E375D, Figures 2A, 3C, and 5C), and five variants whose K3 resistance was improved (E375K, L452S, T487S, T491R, and T496P, Figures 2A and 5C).

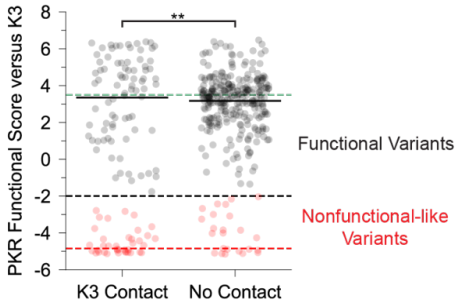

Supplemental Figure 5. Bimodal distribution of PKR functional scores at K3 contact sites. Strip plot of PKR functional scores versus K3 partitioned by predicted contact with K3. Black dashed line denotes the threshold at which variants were separated as nonfunctional-like or functional. Green and red dashed lines represent mean scores for WT PKR and nonsense variants. (** $p < 0.01$, two-sample t-test, comparing just the variants classified as functional in the two classes.)

```
                                                                  #
                  0         10        20        30        40        50
Human eIF2α       MPGLSCRFYQHKFPEVEDVVMVNVRSIAEMGAYVSLLEYNNIEGMILLSELSR--RRIRS
                       1        10        20         30        40        50
Vaccinia K3       -----MLAFCYSLPNAGDVIKGRVYE-KDYALYIYLFDYPHFEAILAESVKMHMDRYVEY
                           : :.:*:. **:  .* .  : . *: *::* ::*.::  *   .  * :

                    60        70        80        90        100       110
Human eIF2α       INKLIRIGRNECVVVIRVDKEKGYIDLSKRRVSPEEAIKCEDKFTKSKTVYSILRHVAEV
                  55     60        70        80
Vaccinia K3       RDKL--VGKTVKVKVIRVDYTKGYIDVNYKRMCRHQ------------------------
                   :**  :*..  * *****  *****:. .*:.  :
```

Supplemental Figure 6. Sequence similarity between human eIF2α and vaccinia K3. Alignment of human eIF2α (RefSeq Accession NP_004085.1, residues 0-117) to vaccinia K3 (RefSeq Accession YP_232916.1). The Ser51 site of phosphorylation in eIF2α is indicated by #. Sequences were aligned using Muscle 3.8 and displayed in Clustal format, * = fully conserved, : = strong group conservation, . = weak group conservation. Sites 41-58 of K3 correspond to the rigid helix insert, which is proximal to PKR's ATP-binding site in the Alphafold2-predicted complex, while sites 72-83 are proximal to PKR's helix αG.

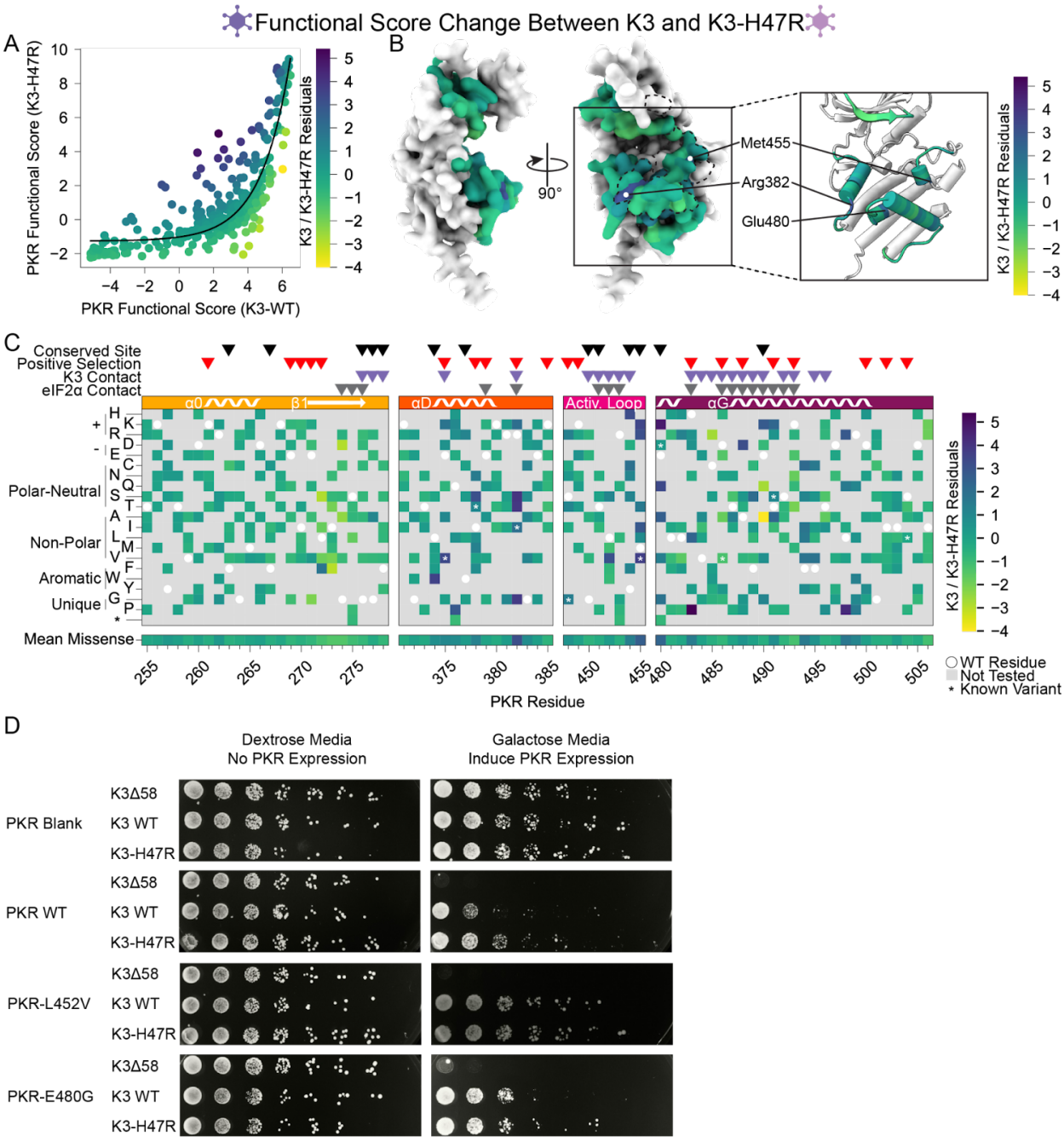

Supplemental Figure 7. Differing patterns of resistance between wild-type K3 and K3-H47R. (A) A nonlinear exponential curve (black line) was fitted to the data in the scatter plot from Figure 5A. Points are colored by their residuals from that curve (K3 / K3-H47R Residuals), ranging from enhanced (purple) to decreased (yellow) resistance to K3-H47R relative to the expectation from K3 resistance. This color scheme is used in panels B and C. (B) Surface structure of PKR kinase domain with sites colored by the mean K3 / K3-H47R residuals for missense variants. The K3 contact site is delineated with a black dashed line. (Inset) Location of K3-H47R-resistant sites where variants deviated most strongly between the wild-type K3 and K3-H47R conditions. (C) Heatmap of PKR variants with cells colored by the K3 / K3-H47R residuals for each variant. (D) Two PKR variants that did not follow the general trend of enhanced susceptibility to K3-H47R relative to K3 WT were selected for validation. The variants

802 were generated and screened against K3Δ58, WT, and H47R alleles using a yeast growth
803 assay visualized through serial dilution as in Supplemental Figure 4.

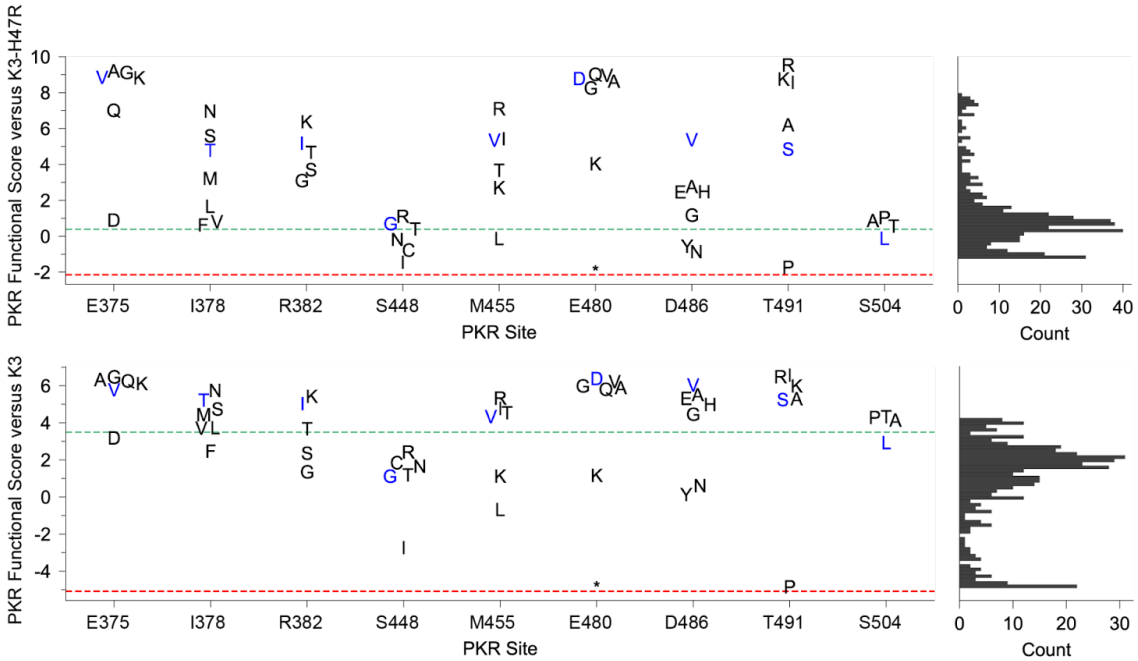

Supplemental Figure 8. Additional variants at the sites of previously identified K3-H47R-resistant variants often also conferred resistance to K3. Strip plots of PKR functional scores of variants paired with K3-H47R (top) and K3-WT (bottom). Each plot highlights PKR variants made at sites where an improved PKR variant was previously identified (24). Blue markers denote previously identified variants; black markers are additional variants made at the same site. Green and red dashed lines represent mean scores for WT PKR and nonsense variants, respectively. Histograms (right) show PKR functional scores versus K3-H47R (top) and K3 (bottom) for all variants. * = stop codon.

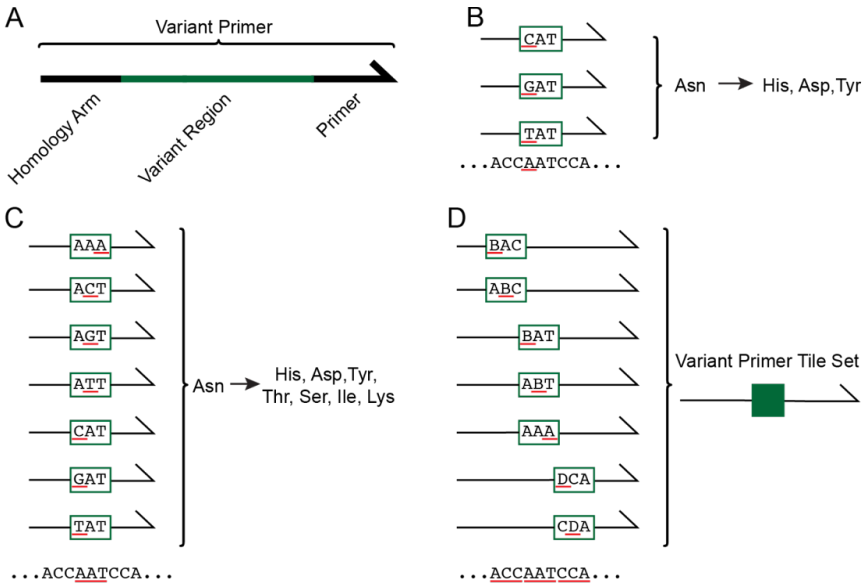

Supplemental Figure 9. Systematic generation of PKR variants using mixed-base primer tile sets. (A) Each variant primer is composed of a homology arm, variant region, and priming region. (B) Nonsynonymous SNP-accessible variants are generated by altering the codon in the variant region of the primer. This example depicts the codon “AAT” encoding Asn. The first nucleotide in the codon, “A”, is underlined in red, with three codons above having changes to “C”, “G”, and “T” underlined in red, which generate the nonsynonymous variants His, Asp, and Tyr. (C) Variant primers were designed across all three nucleotides in each codon, as underlined in red. (D) Variant primer tile sets, represented in dark green, were made by pooling variant primers that modify adjacent codons. Primers included in a given variant primer tile sets have differing variant regions but share homology arms and priming region sequences.

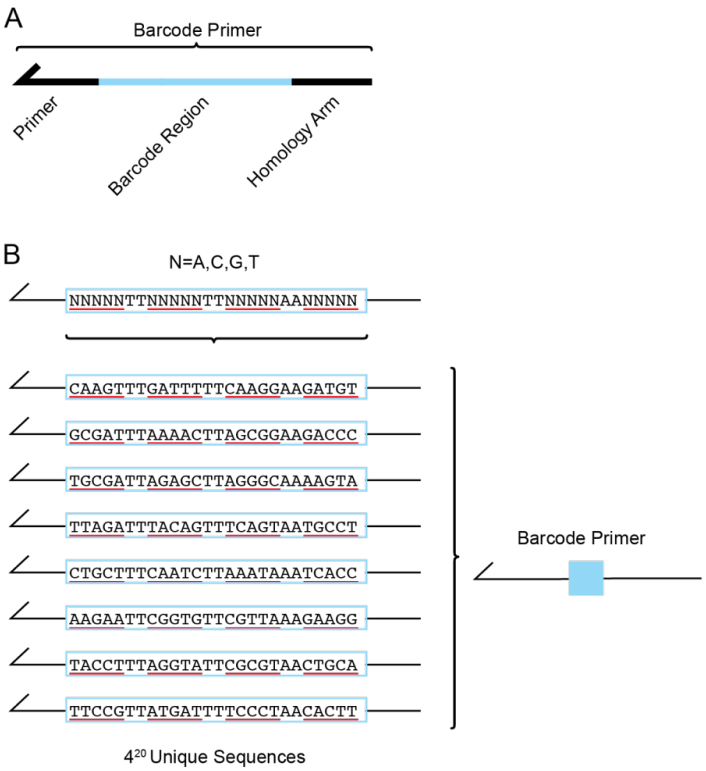

Supplemental Figure 10. Multiple unique barcode sequences were attached to each PKR variant. (A) The barcode primer is composed of a homology arm, barcode region, and priming region. The barcode primer is used as the reverse primer in the variant-generating PCR reactions to attach a unique nucleotide sequence after the PKR variant sequence. (B) The barcode region of the primer is composed of 20 “N”, representing an equal mix of the nucleotides “A”, “C”, “G”, and “T”. A barcode primer with 20 random nucleotides can take on 4^{20} unique nucleotide sequences. Dinucleotide sequences “TT” and “AA” are interspersed throughout the barcode region to avoid making unintended restriction enzyme cut sites.

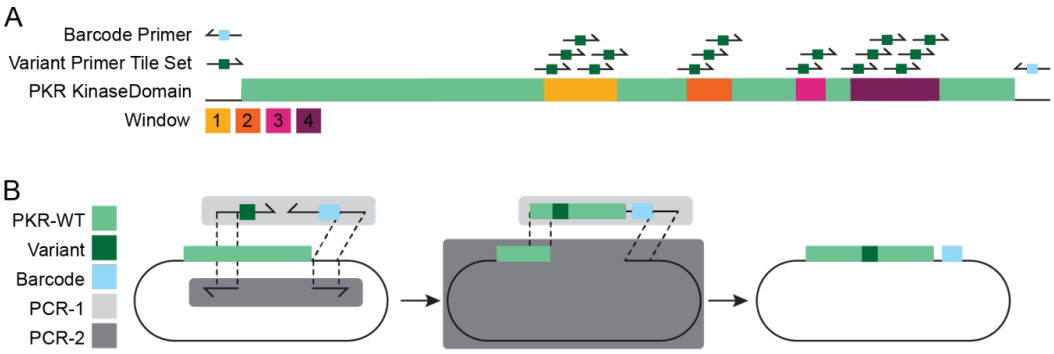

Supplemental Figure 11. Assembly of PKR variant library using variant tile sets and barcode primers. (A) 15 variant primer tile sets were designed to generate variants across four windows of interest in PKR. The full-length PKR sequence is denoted in green, with Windows 1-4 overlaid in yellow, orange, magenta, and burgundy, respectively. Variant primer tile sets were used to generate 426 PKR missense variants, for a total of 15 PCR-1 reactions. (B) Two separate PCR reactions were used to generate complementary insert and vector fragments. PCR-1 primers (light gray box) include a single variant primer tile set (dark green, see Supplemental Figure 9) and a single doped barcode primer (light blue, see Supplemental Figure 10) that amplified from WT PKR (green) and made the PCR-1 insert fragment containing a select nonsynonymous variants (dark green) and a unique barcodes (blue). PCR-2 primers included a single forward and reverse primer that amplified from WT PKR and made a larger vector fragment with 20-bp homology arms that complement the homology arms of the PCR-1 insert fragment. The two fragments were combined via Gibson Assembly to form a pool of complete vectors, each vector containing a single, nonsynonymous variant with a unique barcode.

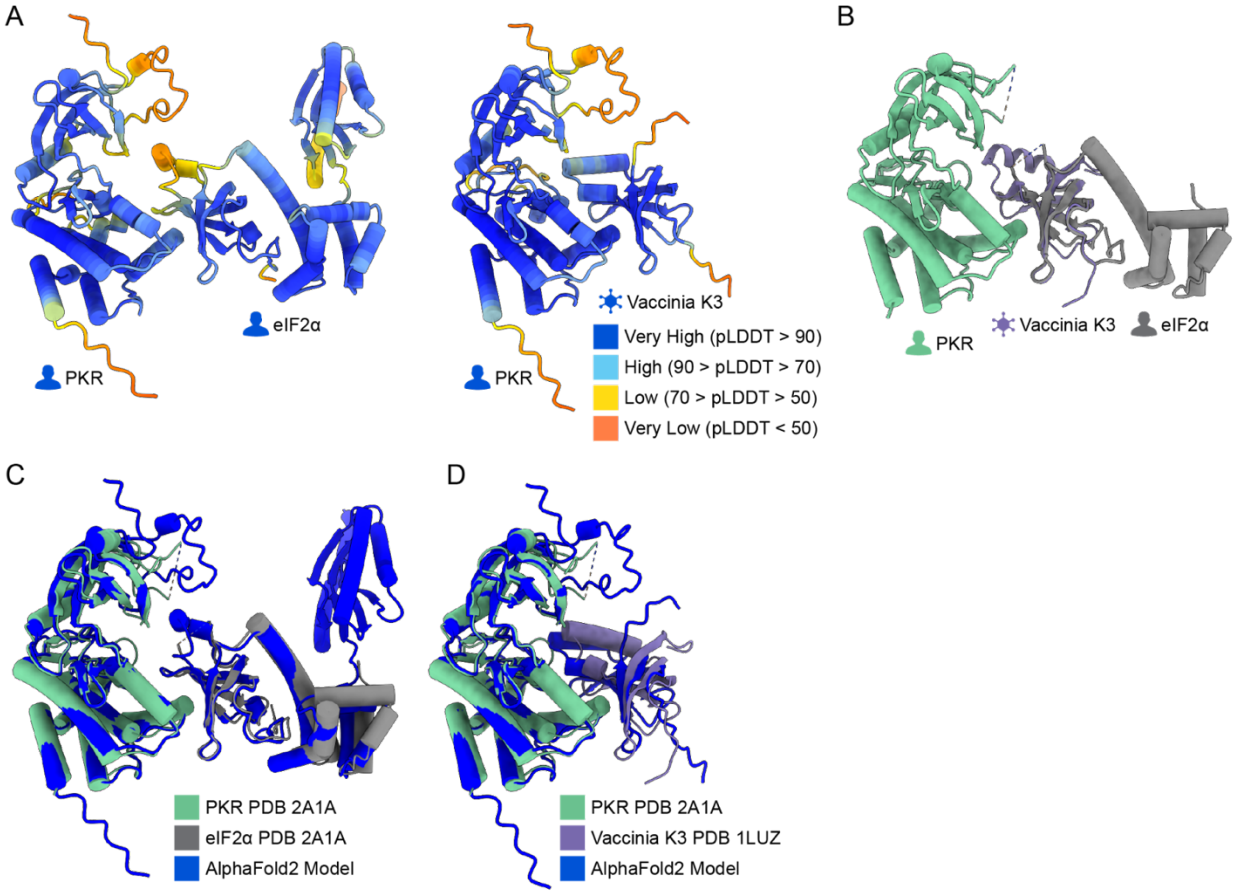

Supplemental Figure 12. Alphafold2 Multimer predictions used to identify PKR sites proximal to eIF2α and K3. (A) AlphaFold2 Multimer prediction of PKR in complex with eIF2α (Left) and K3 (Right). Residues are colored by AlphaFold2 pLDDT confidence scores per residue. In both predicted models, PKR is on the left and its binding partner is on the right, as in Figure 1A,B. (B) Crystal structure of PKR (green, PDB 2A1A) in complex with eIF2α (gray, PDB 2A1A) with the crystal structure of vaccinia K3 (purple, PDB 1LUZ) aligned to eIF2α (root-mean-square deviation (RMSD) = 0.819 Å). (C) Overlay of the PKR-eIF2a from PDB 2A1A (green and gray) and AlphaFold2 (blue), RMSD = 0.970 Å. (D) Overlay of the PKR-Vaccinia K3 complex from PDB 2A1A and 1LUZ (green and purple) to AlphaFold2 (blue), RMSD = 0.944 Å.

SUPPLEMENTAL DATA

Supplementary File 1 - 1_Oligo-Table.xlsx
Supplementary File 2 - 2_Variant-Primers.xlsx
Supplementary File 3 - 3_Plasmids.xlsx
Supplementary File 4 - 4_PKR-Functional-Scores.csv
Supplementary File 5 - 5_Structure-Alignment-RMSD-Values.xlsx
Supplementary File 6 - 6_AF2_PKR-KD_eIF2a.pdb
Supplementary File 7 - 7_AF2_PKR-KD_VACV-K3.pdb

REFERENCES

1. Daugherty MD, Malik HS. Rules of Engagement: Molecular Insights from Host-Virus Arms Races. Annual Review of Genetics. 2012;46(1):677–700.
2. Metz DH, Esteban M. Interferon inhibits Viral Protein Synthesis in L Cells infected with Vaccinia Virus. Nature. 1972 Aug;238(5364):385–8.
3. Clemens MJ. PKR—A protein kinase regulated by double-stranded RNA. The International Journal of Biochemistry & Cell Biology. 1997 Jul 1;29(7):945–9.
4. Balachandran S, Roberts PC, Brown LE, Truong H, Pattnaik AK, Archer DR, et al. Essential Role for the dsRNA-Dependent Protein Kinase PKR in Innate Immunity to Viral Infection. Immunity. 2000 Jul 1;13(1):129–41.
5. Dar AC, Dever TE, Sicheri F. Higher-Order Substrate Recognition of eIF2α by the RNA-Dependent Protein Kinase PKR. Cell. 2005 Sep 23;122(6):887–900.
6. Weber F, Wagner V, Rasmussen SB, Hartmann R, Paludan SR. Double-Stranded RNA Is Produced by Positive-Strand RNA Viruses and DNA Viruses but Not in Detectable Amounts by Negative-Strand RNA Viruses. Journal of Virology. 2006 May 15;80(10):5059–64.
7. Meurs E, Chong K, Galabru J, Thomas NSB, Kerr IM, Williams BRG, et al. Molecular cloning and characterization of the human double-stranded RNA-activated protein kinase induced by interferon. Cell. 1990 Jul 27;62(2):379–90.
8. Kaufman RJ. Double-stranded RNA-activated protein kinase PKR. Cold Spring Harbor Monograph Series. 2000;39:503–28.
9. Dey M, Cao C, Dar AC, Tamura T, Ozato K, Sicheri F, et al. Mechanistic Link between PKR Dimerization, Autophosphorylation, and eIF2α Substrate Recognition. Cell. 2005 Sep 23;122(6):901–13.
10. Lemaire PA, Anderson E, Lary J, Cole JL. Mechanism of PKR Activation by dsRNA. Journal of molecular biology. 2008;381(2):351–60.
11. Hershey JWB. Translational Control in Mammalian Cells. Annu Rev Biochem. 1991 Jun;60(1):717–55.
12. Sudhakar A, Ramachandran A, Ghosh S, Hasnain SE, Kaufman RJ, Ramaiah KVA. Phosphorylation of Serine 51 in Initiation Factor 2α (eIF2α) Promotes Complex Formation between eIF2α(P) and eIF2B and Causes Inhibition in the Guanine Nucleotide Exchange Activity of eIF2B. Biochemistry. 2000 Oct 1;39(42):12929–38.
13. Rothenburg S, Seo EJ, Gibbs JS, Dever TE, Dittmar K. Rapid evolution of protein kinase PKR alters sensitivity to viral inhibitors. Nature Structural & Molecular Biology. 2009 Jan;16(1):63–70.
14. Elde NC, Child SJ, Geballe AP, Malik HS. Protein kinase R reveals an evolutionary model for defeating viral mimicry. Nature. 2009 Jan;457(7228):485–9.
15. Langland JO, Cameron JM, Heck MC, Jancovich JK, Jacobs BL. Inhibition of PKR by RNA and DNA viruses. Virus research. 2006;119(1):100–10.
16. Nallagatla SR, Toroney R, Bevilacqua PC. Regulation of innate immunity through RNA structure and the protein kinase PKR. Curr Opin Struct Biol. 2011 Feb;21(1):119–27.
17. Hull CM, Bevilacqua PC. Discriminating Self and Non-Self by RNA: Roles for RNA Structure, Misfolding, and Modification in Regulating the Innate Immune Sensor PKR. Acc Chem Res. 2016 Jun 21;49(6):1242–9.
18. Beattie E, Tartaglia J, Paoletti E. Vaccinia virus-encoded eIF-2α homolog abrogates the antiviral effect of interferon. Virology. 1991;183(1):419–22.
19. Carroll K, Elroy-Stein O, Moss B, Jagus R. Recombinant vaccinia virus K3L gene product prevents activation of double-stranded RNA-dependent, initiation factor 2 alpha-specific protein kinase. Journal of Biological Chemistry. 1993 Jun 15;268(17):12837–42.
20. Davies MV, Chang HW, Jacobs BL, Kaufman RJ. The E3L and K3L vaccinia virus gene products stimulate translation through inhibition of the double-stranded RNA-dependent protein kinase by different mechanisms. Journal of Virology. 1993 Mar;67(3):1688–92.

21. Sharp TV, Witzel JE, Jagus R. Homologous Regions of the α Subunit of Eukaryotic Translational Initiation Factor 2 (eIF2α) and the Vaccinia Virus K3L Gene Product Interact with the Same Domain within the dsRNA-Activated Protein Kinase (PKR). European Journal of Biochemistry. 1997;250(1):85–91.
22. Dar AC, Sicheri F. X-Ray Crystal Structure and Functional Analysis of Vaccinia Virus K3L Reveals Molecular Determinants for PKR Subversion and Substrate Recognition. Molecular Cell. 2002 Aug 1;10(2):295–305.
23. Kawagishi-Kobayashi M, Silverman JB, Ung TL, Dever TE. Regulation of the protein kinase PKR by the vaccinia virus pseudosubstrate inhibitor K3L is dependent on residues conserved between the K3L protein and the PKR substrate eIF2alpha. Molecular and Cellular Biology. 1997 Jul 1;17(7):4146–58.
24. Seo EJ, Liu F, Kawagishi-Kobayashi M, Ung TL, Cao C, Dar AC, et al. Protein kinase PKR mutants resistant to the poxvirus pseudosubstrate K3L protein. Proceedings of the National Academy of Sciences. 2008 Nov 4;105(44):16894–9.
25. Chong K l., Feng L, Schappert K, Meurs E, Donahue T f., Friesen J d., et al. Human p68 kinase exhibits growth suppression in yeast and homology to the translational regulator GCN2. The EMBO Journal. 1992 Apr 1;11(4):1553–62.
26. Dever TE, Chen JJ, Barber GN, Cigan AM, Feng L, Donahue TF, et al. Mammalian eukaryotic initiation factor 2 alpha kinases functionally substitute for GCN2 protein kinase in the GCN4 translational control mechanism of yeast. PNAS. 1993 May 15;90(10):4616–20.
27. Elde NC, Child SJ, Eickbush MT, Kitzman JO, Rogers KS, Shendure J, et al. Poxviruses Deploy Genomic Accordions to Adapt Rapidly against Host Antiviral Defenses. Cell. 2012 Aug 17;150(4):831–41.
28. Dey M, Velyvis A, Li JJ, Chiu E, Chiovitti D, Kay LE, et al. Requirement for kinase-induced conformational change in eukaryotic initiation factor 2α (eIF2α) restricts phosphorylation of Ser51. Proceedings of the National Academy of Sciences. 2011 Mar 15;108(11):4316–21.
29. Haller SL, Peng C, McFadden G, Rothenburg S. Poxviruses and the evolution of host range and virulence. Infection, Genetics and Evolution. 2014 Jan 1;21:15–40.
30. Rothenburg S, Chinchar VG, Dever TE. Characterization of a ranavirus inhibitor of the antiviral protein kinase PKR. BMC Microbiology. 2011 Mar 18;11(1):56.
31. Sawyer SL, Wu LI, Emerman M, Malik HS. Positive selection of primate TRIM5α identifies a critical species-specific retroviral restriction domain. Proceedings of the National Academy of Sciences. 2005 Feb 22;102(8):2832–7.
32. Tenthorey JL, Young C, Sodeinde A, Emerman M, Malik HS. Mutational resilience of antiviral restriction favors primate TRIM5α in host-virus evolutionary arms races. Schoggins JW, Weigel D, Berthoux L, editors. eLife. 2020 Sep 15;9:e59988.
33. Colón-Thillet R, Hsieh E, Graf L, McLaughlin RN, Young JM, Kochs G, et al. Combinatorial mutagenesis of rapidly evolving residues yields super-restrictor antiviral proteins. PLoS Biol. 2019;17(10):e3000181.
34. Chavarría-Smith J, Mitchell PS, Ho AM, Daugherty MD, Vance RE. Functional and Evolutionary Analyses Identify Proteolysis as a General Mechanism for NLRP1 Inflammasome Activation. PLOS Pathogens. 2016 Dec 7;12(12):e1006052.
35. Demogines A, Farzan M, Sawyer SL. Evidence for ACE2-Utilizing Coronaviruses (CoVs) Related to Severe Acute Respiratory Syndrome CoV in Bats. Journal of Virology. 2012 Jun 1;86(11):6350–3.
36. Damas J, Hughes GM, Keough KC, Painter CA, Persky NS, Corbo M, et al. Broad host range of SARS-CoV-2 predicted by comparative and structural analysis of ACE2 in vertebrates. PNAS. 2020 Sep 8;117(36):22311–22.
37. Frank HK, Enard D, Boyd SD. Exceptional diversity and selection pressure on coronavirus host receptors in bats compared to other mammals. Proc Biol Sci. 289(1979):20220193.

38. Lan J, Ge J, Yu J, Shan S, Zhou H, Fan S, et al. Structure of the SARS-CoV-2 spike receptor-binding domain bound to the ACE2 receptor. Nature. 2020 May;581(7807):215–20.
39. Chan KK, Dorosky D, Sharma P, Abbasi SA, Dye JM, Kranz DM, et al. Engineering human ACE2 to optimize binding to the spike protein of SARS coronavirus 2. Science. 2020 Sep 4;369(6508):1261–5.
40. Heinzelman P, Romero PA. Discovery of human ACE2 variants with altered recognition by the SARS-CoV-2 spike protein. PLOS ONE. 2021 May 12;16(5):e0251585.
41. Chen S, Francioli LC, Goodrich JK, Collins RL, Kanai M, Wang Q, et al. A genomic mutational constraint map using variation in 76,156 human genomes. Nature. 2024 Jan;625(7993):92–100.
42. Jacquet S, Culbertson M, Zhang C, El Filali A, De La Myre Mory C, Pons JB, et al. Adaptive duplication and genetic diversification of protein kinase R contribute to the specificity of bat-virus interactions. Science Advances. 2022 Nov 23;8(47):eadd7540.
43. Siekierka J, Manne V, Ochoa S. Mechanism of translational control by partial phosphorylation of the alpha subunit of eukaryotic initiation factor 2. Proceedings of the National Academy of Sciences. 1984 Jan;81(2):352–6.
44. Ogden PJ, Kelsic ED, Sinai S, Church GM. Comprehensive AAV capsid fitness landscape reveals a viral gene and enables machine-guided design. Science. 2019 Nov 29;366(6469):1139–43.
45. Parvez S, Herdman C, Beerens M, Chakraborti K, Harmer ZP, Yeh JRJ, et al. MIC-Drop: A platform for large-scale in vivo CRISPR screens. Science. 2021 Sep 3;373(6559):1146–51.
46. Popp NA, Powell RL, Wheelock MK, Zapp BD, Holmes KJ, Sheldon KM, et al. Multiplex, multimodal mapping of variant effects in secreted proteins [Internet]. bioRxiv; 2024 [cited 2024 Apr 30]. p. 2024.04.01.587474. Available from: https://www.biorxiv.org/content/10.1101/2024.04.01.587474v1
47. Park C, Peng C, Brennan G, Rothenburg S. Species-specific inhibition of antiviral protein kinase R by capripoxviruses and vaccinia virus. Annals of the New York Academy of Sciences. 2019;1438(1):18–29.
48. Park C, Peng C, Rahman MJ, Haller SL, Tazi L, Brennan G, et al. Orthopoxvirus K3 orthologs show virus- and host-specific inhibition of the antiviral protein kinase PKR. PLOS Pathogens. 2021 Jan 14;17(1):e1009183.
49. Peng C, Haller SL, Rahman MM, McFadden G, Rothenburg S. Myxoma virus M156 is a specific inhibitor of rabbit PKR but contains a loss-of-function mutation in Australian virus isolates. PNAS. 2016 Apr 5;113(14):3855–60.
50. Smith GL. Genus Orthopoxvirus: Vaccinia virus. In: Mercer AA, Schmidt A, Weber O, editors. Poxviruses [Internet]. Basel: Birkhäuser; 2007 [cited 2024 Sep 18]. p. 1–45. Available from: https://doi.org/10.1007/978-3-7643-7557-7_1
51. Rose MD, Novick P, Thomas JH, Botstein D, Fink GR. A *Saccharomyces cerevisiae* genomic plasmid bank based on a centromere-containing shuttle vector. Gene. 1987 Jan 1;60(2):237–43.
52. Curran KA, Morse NJ, Markham KA, Wagman AM, Gupta A, Alper HS. Short Synthetic Terminators for Improved Heterologous Gene Expression in Yeast. ACS Synth Biol. 2015 Jul 17;4(7):824–32.
53. Brachmann CB, Davies A, Cost GJ, Caputo E, Li J, Hieter P, et al. Designer deletion strains derived from Saccharomyces cerevisiae S288C: A useful set of strains and plasmids for PCR-mediated gene disruption and other applications. Yeast. 1998;14(2):115–32.
54. Liu X, Liu Z, Dziulko AK, Li F, Miller D, Morabito RD, et al. iSeq 2.0: A Modular and Interchangeable Toolkit for Interaction Screening in Yeast. Cell Systems. 2019 Apr 24;8(4):338-344.e8.
55. Cornish-Bowden A. Nomenclature for incompletely specified bases in nucleic acid sequences: recommendations 1984. Nucleic acids research. 1985;13(9):3021.
56. Guido VR, Drake Jr FL. Python 3 reference manual. Scotts Valley: CreateSpace. 2009;

57. Crawford KH d, Bloom JD. alignparse: A Python package for parsing complex features from high-throughput long-read sequencing. Journal of Open Source Software. 2019 Dec 11;4(44):1915.
58. Sambrook J, Russell DW. Standard Ethanol Precipitation of DNA in Microcentrifuge Tubes. Cold Spring Harb Protoc. 2006 Jun 1;2006(1):pdb.prot4456.
59. Gietz RD, Schiestl RH. Large-scale high-efficiency yeast transformation using the LiAc/SS carrier DNA/PEG method. Nat Protoc. 2007;2(1):38–41.
60. Singh MV, Anthony Weil P. A method for plasmid purification directly from yeast. Analytical Biochemistry. 2002 Aug 1;307(1):13–7.
61. Wu L, Wen C, Qin Y, Yin H, Tu Q, Van Nostrand JD, et al. Phasing amplicon sequencing on Illumina Miseq for robust environmental microbial community analysis. BMC Microbiol. 2015 Dec;15(1):1–12.
62. Zhang J, Kobert K, Flouri T, Stamatakis A. PEAR: a fast and accurate Illumina Paired-End reAd mergeR. Bioinformatics. 2014 Mar 1;30(5):614–20.
63. Zhao L, Liu Z, Levy SF, Wu S. Bartender: a fast and accurate clustering algorithm to count barcode reads. Bioinformatics. 2018 Mar 1;34(5):739–47.
64. Meng EC, Goddard TD, Pettersen EF, Couch GS, Pearson ZJ, Morris JH, et al. UCSF ChimeraX: Tools for structure building and analysis. Protein Science. 2023;32(11):e4792.
65. Mirdita M, Schütze K, Moriwaki Y, Heo L, Ovchinnikov S, Steinegger M. ColabFold: making protein folding accessible to all. Nat Methods. 2022 Jun;19(6):679–82.
66. Dhaliwal S, Hoffman DW. The Crystal Structure of the N-terminal Region of the Alpha Subunit of Translation Initiation Factor 2 (eIF2α) from *Saccharomyces cerevisiae* Provides a View of the Loop Containing Serine 51, the Target of the eIF2α-specific Kinases. Journal of Molecular Biology. 2003 Nov 21;334(2):187–95.